Numerical study of the three-boson bound-state problem in partial-wave and vector-variable formulations

Wolfgang Schadow*
Caribou3D Research & Development
53424 Remagen, Kirchplatz 1, Germany
(Dated: June 3, 2026)

We present a systematic benchmark of the three-boson bound-state problem in momentum space, comparing one-dimensional (1D) spectator-amplitude, two-dimensional (2D) partial-wave, and three-dimensional (3D) vector-variable formulations. The benchmark controls the interaction representation by embedding the same finite partial-wave interaction space in each formulation, so that discrepancies reflect discretization, interpolation, and quadrature errors. This enables direct 1D–2D–3D comparisons for separable interactions, controlled 2D–3D tests for local interactions, and comparison with the full local interaction in the 3D vector-variable formulation. Binding energies agree at the 10^{-6} MeV level for separable interactions and at the few-10^{-6} to 10^{-5} MeV level for local interactions. The 2D and 3D equations are also solved in both t-matrix-driven and bare-potential-driven forms, whose agreement validates the permutation geometry, quadrature, and interpolation. Fourier transforms to coordinate space yield consistent norm decompositions and spatial observables, providing an independent check of the momentum-space solutions.

PACS numbers: 21.45.-v, 03.65.Ge, 02.60.Nm, 03.65.Nk
Keywords: Three-body bound state, Lippmann–Schwinger equation, Momentum space, Vector variables, Partial-wave decomposition, Yamaguchi potential, Malfliet–Tjon potential, Numerical benchmarks

arXiv:2606.05028v1 [nucl-th] 3 Jun 2026

I. INTRODUCTION

The quantitative description of quantum systems with three or more interacting particles remains a central problem in few-body physics. In nuclear and atomic systems, this requires the solution of the Faddeev or Faddeev–Yakubovsky equations [1–25]. Their numerical solution is computationally demanding due to the nontrivial integral kernels and permutation operators. Establishing the reliability of different numerical realizations therefore requires internally consistent benchmark calculations.

A common strategy for testing few-body methods is to apply them to simpler systems for which high-precision or partially analytical solutions are available. For bound states, partial-wave decomposition provides an efficient and well-established framework, reducing the problem to a set of coupled one-dimensional (1D) or two-dimensional (2D) integral equations. However, formulations based directly on vector momentum variables offer an important complementary approach, retaining the full angular dependence of the wave function without explicitly expanding it in partial waves.

Although these three-dimensional (3D) vector-variable approaches avoid a partial-wave decomposition of the wave function, they introduce complex numerical structures. Specifically, the evaluation of multidimensional integrals involving shifted permutation arguments becomes a central computational task. Validating these methods therefore requires benchmarks that rigorously test the underlying multidimensional integration and interpolation schemes.

This work provides a stringent cross-validation framework for 3D vector-variable calculations. The benchmark is constructed by controlling the interaction representation: the same finite partial-wave interaction space is embedded in the different formulations, so that remaining discrepancies reflect discretization, interpolation, and quadrature errors. For separable Yamaguchi-type potentials [26], this gives a direct 1D–2D–3D comparison. For local Malfliet–Tjon (MT) potentials [27], it provides a controlled 2D–3D comparison and a test against the full local interaction in the 3D vector-variable formulation.

For both the 2D and 3D calculations, implementing the formally equivalent t-matrix-driven and V-driven Faddeev equations provides an additional consistency check. While algebraically equivalent, they lead to structurally distinct numerical kernels. Their agreement tests the multidimensional permutation geometry, interpolation, and integration schemes.

To extract spatial information from the bound state, the momentum-space wave functions must be transformed into configuration space via Fourier integrals. This introduces an additional layer of numerical complexity due to the highly oscillatory nature of the integrands. To control this, we employ a hybrid Filon-type quadrature [28, 29]—a semi-analytical technique that treats the rapid trigonometric oscillations analytically while interpolating the smooth momentum envelope—yielding a numerically stable transformation. This enables a direct coordinate-space comparison between the partial-wave and vector-variable representations.

The paper is organized as follows. In Sec. II we summarize the general three-body formalism. Sections III and IV present the 1D and 2D formulations, respectively. The 3D vector-variable approach is developed in Sec. V. Numerical details, including the treatment of the oscillatory spatial transformations, are given in Sec. VIII. Results and discussion are presented in Sec. IX, followed by a concluding summary in Sec. X.

*wolfgang.schadow@caribou3d.com

II. THE THREE-BODY BOUND STATE

The bound state of three identical particles interacting via pairwise forces $V_i \equiv V_{jk}$, where (i, j, k) denotes a cyclic permutation of $(1, 2, 3)$, is governed by the Schrödinger equation, which reads in integral form

$$|\Psi\rangle = G_0(E_3) \sum_{i=1}^{3} V_i \, |\Psi\rangle. \tag{1}$$

Here, $G_0(E_3) = (E_3 - H_0)^{-1}$ is the free three-body resolvent at the bound-state energy $E_3 < 0$, and H_0 is the free Hamiltonian. Introducing Faddeev components $|\Psi\rangle = \sum_{i=1}^{3} |\psi_i\rangle$, defined by $|\psi_i\rangle = G_0(E_3)V_i|\Psi\rangle$, and using the embedded two-body transition operator $t_i = V_i + V_i G_0(E_3) t_i$, one obtains the standard set of coupled Faddeev equations

$$|\psi_i\rangle = G_0(E_3)\, t_i \sum_{j \neq i} |\psi_j\rangle, \tag{2}$$

where t_i denotes the two-body t-matrix in subsystem jk.

For a system of identical spinless bosons, the full three-particle wave function $|\Psi\rangle$ must be totally symmetric. The three Faddeev components are generated from one another by particle permutations and therefore have the same functional form in their respective Jacobi coordinate systems. It is thus sufficient to consider a single component,

$$|\psi\rangle = G_0(E_3)\, t\, P\, |\psi\rangle, \tag{3}$$

where the arbitrary component index has been dropped. The permutation operator is given by $P = P_{12}P_{23} + P_{13}P_{23}$. The complete three-boson wave function is subsequently recovered via

$$|\Psi\rangle = (1 + P)\, |\psi\rangle. \tag{4}$$

For the 2D and 3D formulations, it is useful to work with an equivalent equation for the same Faddeev component, driven directly by the bare potential. Starting from the definition $|\psi_1\rangle = G_0(E_3)V_1|\Psi\rangle$ and substituting the sum of components yields

$$|\psi_1\rangle = G_0(E_3)\, V_1 \Big(|\psi_1\rangle + |\psi_2\rangle + |\psi_3\rangle \Big). \tag{5}$$

For identical bosons, $|\psi_2\rangle$ and $|\psi_3\rangle$ are generated from $|\psi_1\rangle$ by cyclic and anticyclic permutations, such that $(|\psi_2\rangle + |\psi_3\rangle) = P|\psi_1\rangle$, with P acting on the component in arrangement 1. Dropping the component index gives the V-driven equation

$$|\psi\rangle = G_0(E_3) V (1 + P)\, |\psi\rangle. \tag{6}$$

This formulation avoids the explicit construction of the fully off-shell two-body t-matrix. Consequently, the bare interaction appears directly in the multidimensional kernel, including the direct $G_0(E_3)V|\psi\rangle$ contribution.

To solve these abstract operator equations numerically, they must be projected onto a well-defined momentum-space basis. The resulting integral equations take different forms depending on the interaction type and the chosen coordinate representation. In the following sections, we construct these projections and define the corresponding basis states for three distinct numerical approaches: a 1D spectator-amplitude formulation for separable interactions, a 2D partial-wave formulation, and a 3D vector-variable formulation in which the wave function is represented directly as a function of Jacobi momentum vectors.

III. ONE-DIMENSIONAL APPROACH

For separable interactions, the one-dimensional approach used here is the spectator-amplitude form of the homogeneous Alt–Grassberger–Sandhas (AGS) equations evaluated at the bound-state pole [30]. We derive this equation directly from the Faddeev operator equation [Eq. (3)] at the three-body binding energy $E_3 < 0$.

To solve the Faddeev equations numerically, we must represent the abstract operators in a well-defined momentum basis. Exploiting identical-particle symmetry, we define the basis states in the Jacobi coordinate system of a single arrangement. We introduce the Jacobi momenta p (the relative momentum within the interacting two-body subsystem) and q (the momentum of the spectator particle relative to the center of mass of the interacting pair). With the mass convention used throughout this work, the free three-body kinetic energy is $H_0 = p^2 + \frac{3}{4}q^2$. The conversion to MeV is performed only when numerical results are reported.

For the partial-wave decomposition, we define the orbital angular momentum l of the two-body subsystem and the orbital angular momentum L of the spectator particle. To avoid confusion with the spectator orbital angular momentum L, the total orbital angular momentum of the three-body system is denoted by $\mathcal{L}$, with its z-projection $\mathcal{M}$.

The partial-wave projected states $|p\, q\, (lL)\mathcal{L}\mathcal{M}\rangle$ form a complete basis for this designated arrangement,

$$1 = \sum_{lL\mathcal{L}\mathcal{M}} \int_0^\infty dp\, p^2 \int_0^\infty dq\, q^2 \times |p\, q\, (lL)\mathcal{L}\mathcal{M}\rangle \langle p\, q\, (lL)\mathcal{L}\mathcal{M}|, \tag{7}$$

and are normalized according to

$$\langle p\, q\, (lL)\mathcal{L}\mathcal{M}|p'\, q'\, (l'L')\mathcal{L}'\mathcal{M}'\rangle = \frac{\delta(p - p')}{p^2} \frac{\delta(q - q')}{q^2} \delta_{ll'}\, \delta_{LL'}\, \delta_{\mathcal{L}\mathcal{L}'}\, \delta_{\mathcal{M}\mathcal{M}'}. \tag{8}$$

For the three-boson ground state considered here, the total orbital angular momentum is $\mathcal{L} = 0$, which requires $L = l$. Consequently, we drop the redundant indices L, $\mathcal{L}$, and $\mathcal{M}$, denoting the basis states compactly as $|p\, q\, l\rangle$.

Assuming the two-body potential is separable in each active partial wave, it can be written as

$$V_l(p, p') = -4\pi\lambda_l\, g_l(p) g_l(p'), \tag{9}$$

where $g_l(p)$ is the momentum-space form factor. The corresponding two-body t-matrix has the same rank-one structure,

$$t_l(p, p'; E) = g_l(p)\, \Delta_l(E)\, g_l(p'), \tag{10}$$

where the reduced propagator $\Delta_l(E)$ contains the full two-body energy dependence. With the convention of Eq. (9) and the Lippmann–Schwinger equation $t = V + VG_0t$, it is given by

$$\Delta_l(E) = -\left[(4\pi\lambda_l)^{-1} + \langle g_l|G_0(E)|g_l\rangle\right]^{-1}. \tag{11}$$

The dimensions of λ_l are fixed by the chosen form-factor normalization.

In the three-body problem, the energy available to the interacting pair depends on the spectator momentum. After projection onto a state with spectator momentum q, the subsystem energy is

$$E_{\rm sub}(q) = E_3 - \frac{3}{4}q^2. \tag{12}$$

Since the three-body bound states considered here lie below the dimer-plus-particle threshold, $E_3 < E_2 < 0$, the subsystem energy remains below the two-body pole for all real spectator momenta. Thus no singularity in $\Delta_l(E_{\rm sub})$ is encountered on the integration contour.

Projecting Eq. (3) onto the momentum basis states $|p\,q\,l\rangle$ and utilizing the separable form of Eq. (10), we obtain the functional form of the Faddeev component

$$\psi_l(p,q) = \frac{g_l(p)}{E_3 - p^2 - \frac{3}{4}q^2}\,\Delta_l\left(E_3 - \tfrac{3}{4}q^2\right) \times \int_0^\infty dp'\,p'^2\,g_l(p')\,\langle p'\,q\,l|P|\psi\rangle. \tag{13}$$

We define the spectator amplitude $F_l(q)$ as the integral over the internal subsystem momentum

$$F_l(q) = \int_0^\infty dp'\,p'^2\,g_l(p')\,\langle p'\,q\,l|P|\psi\rangle. \tag{14}$$

Because the internal momentum p' has been integrated out, this amplitude depends strictly on the spectator momentum q. For a given spectator amplitude $F_l(q)$, the Faddeev component is then given by

$$\psi_l(p,q) = \frac{g_l(p)}{E_3 - p^2 - \frac{3}{4}q^2}\,\Delta_l\left(E_3 - \tfrac{3}{4}q^2\right)F_l(q). \tag{15}$$

To find the integral equation governing $F_l(q)$, we insert a completeness relation in the partial-wave basis into the definition of $F_l(q)$,

$$F_l(q) = \sum_{l'}\int_0^\infty dp'\,p'^2\int_0^\infty dp''\,p''^2\int_0^\infty dq'\,q'^2 \times g_l(p')\,\langle p'\,q\,l|P|p''\,q'\,l'\rangle\,\psi_{l'}(p'',q'). \tag{16}$$

Substituting the functional form of $\psi_{l'}$ from Eq. (15) into this expression yields the one-dimensional integral equation

$$F_l(q) = \sum_{l'}\int_0^\infty dq'\,q'^2\,\mathcal{V}_{ll'}(q,q',E_3) \times \Delta_{l'}\left(E_3 - \tfrac{3}{4}q'^2\right)F_{l'}(q'), \tag{17}$$

where the effective spectator kernel $\mathcal{V}_{ll'}$ is defined by the matrix element

$$\mathcal{V}_{ll'}(q,q',E_3) = \int_0^\infty dp\,p^2\int_0^\infty dp'\,p'^2\,g_l(p) \times \frac{\langle p\,q\,l|P|p'\,q'\,l'\rangle}{E_3 - p'^2 - \frac{3}{4}q'^2}\,g_{l'}(p'). \tag{18}$$

The permutation operator connects the different Jacobi coordinate systems. With the completeness and normalization conventions of Eqs. (7) and (8), the standard partial-wave projected permutation matrix element for identical spinless bosons is [31]

$$\langle p\,q\,l|P|p'\,q'\,l'\rangle = \int_{-1}^{1}dx\,\frac{\delta(p-\pi_1)}{p^{l+2}} \times \frac{\delta(p'-\pi_2)}{p'^{l'+2}}\,G_{ll'}(q,q',x), \tag{19}$$

where the shifted momentum arguments are dictated by the kinematics

$$\pi_1 = \sqrt{\tfrac{1}{4}q^2 + q'^2 + qq'x}$$
$$\pi_2 = \sqrt{q^2 + \tfrac{1}{4}q'^2 + qq'x}\,. \tag{20}$$

The geometric factor $G_{ll'}(q,q',x)$ for spinless identical bosons is provided in Appendix B.

Inserting Eq. (19) into the effective kernel, the Dirac delta distributions collapse the integrations over the subsystem momenta, setting $p = \pi_1$ and $p' = \pi_2$. The radial measure p^2dp cancels the measure-related p^2 part of p^{l+2}, leaving $g_l(\pi_1)/\pi_1^l$; analogously, the p'-integration yields $g_{l'}(\pi_2)/\pi_2^{l'}$. This scaling is numerically stable because the form factors used here behave as $g_l(p) \propto p^l$ near the origin.

After evaluating the free resolvent denominator at $p' = \pi_2$, the remaining integration is purely angular. The reduced spectator kernel thus reduces to a single integral over the angle x

$$\mathcal{V}_{ll'}(q,q',E_3) = \int_{-1}^{1}dx\,\frac{g_l(\pi_1)}{\pi_1^l}\,\frac{g_{l'}(\pi_2)}{\pi_2^{l'}} \times \frac{G_{ll'}(q,q',x)}{E_3 - q^2 - q'^2 - qq'x}\,, \tag{21}$$

where the denominator follows from $\pi_2^2 + \frac{3}{4}q'^2 = q^2 + q'^2 + qq'x$.

Equation (17), driven by this reduced spectator kernel, can now be discretized into a linear eigenvalue problem, reducing the three-body kernel to a set of coupled one-dimensional integral equations in the spectator momentum. The energy E_3 is varied until the corresponding eigenvalue equals unity.

Once the spectator amplitudes $F_l(q)$ are found, the partial-wave Faddeev components $\psi_l(p,q)$ are constructed directly

via Eq. (15). The full three-body wave function $\Psi_l(p,q)$ is then generated via Eq. (4)

$$\Psi_l(p,q) = \psi_l(p,q) + \sum_{l'} \int_{-1}^{1} dx\, \tilde{G}_{ll'}(p,q,x)\, \psi_{l'}(\tilde{\pi}_1, \tilde{\pi}_2)\,. \tag{22}$$

The shifted arguments are

$$\tilde{\pi}_1 = \sqrt{\tfrac{1}{4}p^2 + \tfrac{9}{16}q^2 + \tfrac{3}{4}qpx}, \qquad \tilde{\pi}_2 = \sqrt{p^2 + \tfrac{1}{4}q^2 - qpx}\,. \tag{23}$$

The quantity $\tilde{G}_{ll'}(p,q,x)$, which emerges from applying the permutation operator to construct the full wave function components, can be found in Ref. [32]. The explicit expression for the bosonic case considered here is given in Appendix B.

Enforcing the wave function normalization and utilizing the symmetry of the Faddeev components, the norm is evaluated directly as

$$3\langle\psi|\Psi\rangle = 3\sum_l \int_0^\infty dq\, q^2 \int_0^\infty dp\, p^2 \times \psi_l^*(p,q)\, \Psi_l(p,q) = 1\,. \tag{24}$$

A crucial distinction arises here between the partial-wave content of the interaction and that of the full wave function. Because the Faddeev component ψ is driven directly by the two-body interaction, $\psi_l(p,q)$ is strictly non-zero only for the active partial waves $l \le l_{\max}$ included in the potential. Consequently, the sum in the mixed overlap $3\langle\psi|\Psi\rangle$ terminates exactly at $l_{\max}$. In contrast, the permutation operator in Eq. (22) can generate components outside the active interaction space in the reconstructed full wave function. Evaluating the direct norm $\langle\Psi|\Psi\rangle$ in a partial-wave basis would therefore require summing these induced components, whereas the mixed Faddeev overlap terminates at the active $l_{\max}$.

The full Hamiltonian expectation value is evaluated as

$$\langle H\rangle = 3\langle\psi|H_0|\Psi\rangle + 3\langle\Psi|V_1|\Psi\rangle\,. \tag{25}$$

The first factor of three follows from the identical-particle relation $\langle\Psi|\Psi\rangle = 3\langle\psi|\Psi\rangle$, while the second accounts for the three identical pair interactions. The reduced kinetic-energy matrix element is

$$\langle\psi|H_0|\Psi\rangle = \sum_l \int_0^\infty dp\, p^2 \int_0^\infty dq\, q^2 \left(p^2 + \frac{3}{4}q^2\right) \times \psi_l^*(p,q)\, \Psi_l(p,q)\,, \tag{26}$$

and the matrix element of one pair interaction is

$$\langle\Psi|V_1|\Psi\rangle = \sum_l \int_0^\infty dp\, p^2 \int_0^\infty dq\, q^2 \int_0^\infty dp'\, p'^2 \times \Psi_l^*(p,q)\, V_l(p,p')\, \Psi_l(p',q)\,. \tag{27}$$

In the numerical results below, the consistency of $\langle H\rangle$ with the eigenvalue energy E_3 provides an independent check of the reconstructed full wave function.

IV. TWO-DIMENSIONAL APPROACH

For general non-separable interactions, such as the local Malfliet–Tjon potential used below, the two-body t-matrix cannot be factored into a product of functions depending on single momenta. Consequently, the internal subsystem momentum p cannot be eliminated by a rank-one factorization and remains explicitly coupled to the spectator momentum q. This leads to a two-dimensional (2D) partial-wave formulation.

We begin by projecting the standard Faddeev operator equation [Eq. (3)] onto the partial-wave momentum basis $|p\,q\,(lL)\mathcal{L}\mathcal{M}\rangle$. To transition from the abstract operators to the integral equations, we require the matrix elements of the free propagator, the two-body t-matrix, and the permutation operator.

For central, spin-independent interactions, the free propagator and the two-body t-matrix are diagonal in the spectator momentum q, as well as in the angular momenta l, L, $\mathcal{L}$, and $\mathcal{M}$

$$\langle p\,q\,(lL)\mathcal{L}\mathcal{M}|G_0(E_3)|p'\,q'\,(l'L')\mathcal{L}'\mathcal{M}'\rangle = \frac{\delta(p-p')}{p^2}\,\frac{\delta(q-q')}{q^2} \times \delta_{ll'}\,\delta_{LL'}\,\delta_{\mathcal{L}\mathcal{L}'}\,\delta_{\mathcal{M}\mathcal{M}'}\,\frac{1}{E_3 - p^2 - \frac{3}{4}q^2}\,, \tag{28}$$

$$\langle p\,q\,(lL)\mathcal{L}\mathcal{M}|t|p'\,q'\,(l'L')\mathcal{L}'\mathcal{M}'\rangle = \frac{\delta(q-q')}{q^2}\,\delta_{ll'}\,\delta_{LL'}\,\delta_{\mathcal{L}\mathcal{L}'}\,\delta_{\mathcal{M}\mathcal{M}'} \times t_l\left(p,p';E_3 - \tfrac{3}{4}q^2\right). \tag{29}$$

Because the two-body t-matrix and the bare potential V operate only within the interacting pair, their dynamical matrix elements depend exclusively on the subsystem angular momentum l. The matrix element of the permutation operator P has the same form as in the one-dimensional case, Eq. (19), and the shifted momenta π_1 and π_2 are those defined in Eq. (20).

For the bound state considered here, the total angular momentum is $\mathcal{L} = 0$, which requires $L = l$. We consequently drop the redundant indices L, $\mathcal{L}$, and $\mathcal{M}$ from the basis states and the Faddeev components. Because the two-body t-matrix is diagonal in the spectator momentum, it is evaluated at the subsystem energy $E_3 - \frac{3}{4}q^2$. Inserting completeness relations into the standard Faddeev Eq. (3) and integrating over the delta functions yields the coupled two-dimensional integral

equations

$$\psi_l(p,q) = \frac{1}{E_3 - p^2 - \frac{3}{4}q^2} \times \sum_{l'} \int_0^\infty dq'\, q'^2 \int_{-1}^{1} dx'\, \frac{t_l\left(p, \pi_1; E_3 - \frac{3}{4}q^2\right)}{\pi_1^l} \times G_{ll'}(q,q',x')\, \frac{\psi_{l'}(\pi_2, q')}{\pi_2^{l'}}\,. \tag{30}$$

The factors π_1^{-l} and $\pi_2^{-l'}$ originate from the normalization convention used in the partial-wave permutation matrix element, Eq. (19). For identical spinless bosons with central interactions, only even values of l contribute. In numerical calculations, this infinite set is truncated at a sufficiently high value of $l_{\max}$.

The t-driven equation contains only the exchange term $G_0 t P|\psi\rangle$, because the multiple scattering inside the interacting pair is already summed into t_l. In contrast, the potential-driven equation contains both the direct term $G_0 V|\psi\rangle$ and the exchange term $G_0 V P|\psi\rangle$. At the operator level, the equality of the resulting bound-state solutions follows directly from the Faddeev definition $|\psi\rangle = G_0 V(1+P)|\psi\rangle$, whereas the t-driven form is obtained after resumming repeated pair interactions into the two-body transition operator. The two-body potential shares the same spectator-diagonal structure as the t-matrix,

$$\langle p\, q\, l|V|p'\, q'\, l'\rangle = \frac{\delta(q-q')}{q^2}\, \delta_{ll'}\, V_l(p,p')\,. \tag{31}$$

Evaluating the direct term gives an interaction that changes only the subsystem momentum, leaving the spectator momentum q unchanged. In the exchange term, the integration over the intermediate subsystem momentum evaluates the product of $V_l(p,p'')$ and the permutation matrix element $\langle p''\, q\, l|P|p'\, q'\, l'\rangle$. The Dirac delta distributions in the permutation matrix element collapse the subsystem momentum integrals, setting $p'' = \pi_1$ and $p' = \pi_2$.

Consequently, the exchange part of the V-driven equation has the same permutation structure as Eq. (30), with t_l replaced by V_l. The full V-driven equation additionally contains the direct potential term

$$\psi_l(p,q) = \frac{1}{E_3 - p^2 - \frac{3}{4}q^2}\Bigg[\int_0^\infty dp'\, p'^2\, V_l(p,p')\, \psi_l(p',q) + \sum_{l'} \int_0^\infty dq'\, q'^2 \int_{-1}^{1} dx'\, \frac{V_l(p,\pi_1)}{\pi_1^l}\, G_{ll'}(q,q',x') \times \frac{\psi_{l'}(\pi_2,q')}{\pi_2^{l'}}\Bigg]. \tag{32}$$

This formulation shows that the bare potential can drive the three-body system using the same permutation geometry as the t-driven approach, while avoiding the explicit pre-calculation and interpolation of the fully off-shell two-body t-matrix. Depending on the grid sizes and interpolation strategy, this formulation may also reduce the computational cost [33]. Whether determined via the t-driven Eq. (30) or the potential-driven Eq. (32), the resulting Faddeev components $\psi_l(p,q)$ determine the bound state within the chosen partial-wave model space. The full wave function $\Psi_l(p,q)$ is constructed from the Faddeev component as in Eq. (22). The normalization condition $3\langle\psi|\Psi\rangle = 1$ and the Hamiltonian expectation value, Eqs. (25)–(27), are then evaluated in the same way as in Sec. III.

V. THREE-DIMENSIONAL APPROACH

In the three-dimensional (3D) approach, the Faddeev equations are projected directly onto the Jacobi vector momentum states $|\mathbf{p}\,\mathbf{q}\rangle$. Without decomposing the wave function into partial waves, this approach retains the continuous angular dependence between the Jacobi momentum vectors.

To treat the equations numerically in this vector-variable representation, we define the basis states such that they satisfy the completeness relation

$$1 = \int d^3p \int d^3q\; |\mathbf{p}\,\mathbf{q}\rangle\,\langle\mathbf{p}\,\mathbf{q}\,|, \tag{33}$$

and are normalized according to

$$\langle \mathbf{p}\,\mathbf{q}\,|\mathbf{p}'\,\mathbf{q}'\rangle = \delta(\mathbf{p}-\mathbf{p}')\,\delta(\mathbf{q}-\mathbf{q}') = \frac{\delta(p-p')}{p^2}\,\delta(\hat{\mathbf{p}}-\hat{\mathbf{p}}')\,\frac{\delta(q-q')}{q^2}\,\delta(\hat{\mathbf{q}}-\hat{\mathbf{q}}'). \tag{34}$$

Here $\hat{\mathbf{p}}$ and $\hat{\mathbf{q}}$ denote the unit vectors specified by the solid angles $\Omega_{p,q} = (\theta,\varphi)$. Detailed geometric derivations for projecting operators onto this vector basis can be found in Ref. [4].

Before constructing the three-body equations, it is instructive to define the two-body transition operator in this 3D vector-variable basis. Two-body scattering is governed by the Lippmann–Schwinger equation $t = V + V g_0 t$, where g_0 denotes the two-body free resolvent. Restricting to nonrelativistic, local potentials and spinless particles, the matrix elements depend only on the magnitudes of the initial and final momenta and the angle between them.

Specifically, we define the variables $x' = \hat{\mathbf{p}}'\cdot\hat{\mathbf{p}}$, $x'' = \hat{\mathbf{p}}''\cdot\hat{\mathbf{p}}$, and $y = \hat{\mathbf{p}}'\cdot\hat{\mathbf{p}}''$. The explicit integral equation reads

$$t(p',p,x';E) = V(p',p,x') + \int_0^\infty dp''\, p''^2 \int_{-1}^{1} dx'' \int_0^{2\pi} d\varphi'' \times \frac{V(p',p'',y)}{E - p''^2}\, t(p'',p,x'';E), \tag{35}$$

where the internal angle y is expressed via the azimuthal angle φ'' as $y = x'x'' + \sqrt{1-x'^2}\,\sqrt{1-x''^2}\,\cos\varphi''$.

By defining the azimuthally integrated potential

$$v(p',p'',x',x'') \equiv \int_0^{2\pi} d\varphi'' \times V\Big(p',p'',x'x'' + \sqrt{1-x'^2}\,\sqrt{1-x''^2}\,\cos\varphi''\Big), \tag{36}$$

Eq. (35) reduces to a 2D integral equation in p' and x', driven by the azimuthally integrated potential, with the inhomogeneous term evaluated at $p'' = p$ and $x'' = 1$

$$t(p',p,x';E) = \frac{1}{2\pi}\, v(p',p,x',1) + \int_0^\infty dp''\, p''^2 \int_{-1}^{1} dx'' \times \frac{v(p',p'',x',x'')}{E - p''^2}\, t(p'',p,x'';E). \quad (37)$$

This isolates the azimuthal geometry entirely within the azimuthally integrated potential v, a technique we now apply directly to the three-body equations.

Projecting the standard t-driven Faddeev Eq. (3) onto the vector basis and choosing the spectator momentum $\mathbf{q}$ along the z-axis, the Faddeev component depends on p, q, and $x = \hat{\mathbf{p}} \cdot \hat{\mathbf{q}}$. In the following integral, $x' = \hat{\mathbf{q}}' \cdot \hat{\mathbf{q}}$ and φ' is the azimuthal angle of $\mathbf{q}'$ around $\mathbf{q}$. These three-body angular variables should not be confused with the variables used above in the two-body Lippmann–Schwinger equation. This projection yields the 3D integral equation

$$\psi(p,q,x) = \frac{1}{E_3 - p^2 - \frac{3}{4}q^2} \int_0^\infty dq'\, q'^2 \int_{-1}^{1} dx' \int_0^{2\pi} d\varphi' \times t_s\left(p, \pi_1, \frac{\frac{1}{2}qx + q'y}{\pi_1}; E_3 - \tfrac{3}{4}q^2\right) \times \psi\left(\pi_2, q', \frac{qx' + \frac{1}{2}q'}{\pi_2}\right), \quad (38)$$

where t_s denotes the symmetrized two-body t-matrix

$$\langle \mathbf{p}|t_s(E)|\mathbf{q}\rangle = \langle \mathbf{p}|t(E)|\mathbf{q}\rangle + \langle \mathbf{p}|t(E)|-\mathbf{q}\rangle \quad (39)$$

which implements the exchange symmetry of the two particles in the interacting pair.

The shifted momentum magnitudes π_1 and π_2 naturally emerge from the vector addition, taking the same form defined for the 1D permutation in Eq. (20), and the internal angular coupling is given by $y = xx' + \sqrt{1-x^2}\sqrt{1-x'^2}\cos\varphi'$.

Alternatively, projecting the potential-driven Eq. (6) onto the same vector basis produces a structural form that explicitly separates the direct potential interaction from the geometric permutation. Because the potential V in the direct term acts only on the subsystem momentum p, the spectator momentum q is strictly conserved across this interaction.

As in the 2D formulation, the bare potential is diagonal in the spectator momentum. In the direct term this leaves q unchanged, while in the exchange term the shifted Jacobi momenta enter through the same permutation geometry as in the t-driven equation. In the direct term, the integration over the azimuthal angle of the intermediate subsystem momentum is already contained in the azimuthally integrated potential v, so that no additional azimuthal integration appears. Utilizing v defined in Eq. (36) for the direct term, and replacing the t-matrix with the symmetrized bare potential V_s in the permutation term, the V-driven 3D equation becomes

$$\psi(p,q,x) = \frac{1}{E_3 - p^2 - \frac{3}{4}q^2} \left[\int_0^\infty dp'\, p'^2 \int_{-1}^{1} dx'\, v(p,p',x,x')\, \psi(p',q,x') + \int_0^\infty dq'\, q'^2 \int_{-1}^{1} dx' \int_0^{2\pi} d\varphi'\, V_s\left(p, \pi_1, \frac{\frac{1}{2}qx + q'y}{\pi_1}\right) \psi\left(\pi_2, q', \frac{qx' + \frac{1}{2}q'}{\pi_2}\right) \right]. \quad (40)$$

This formulation mirrors the structure of the 2D potential-driven Eq. (32). The bare potential drives the three-body system through the same permutation geometry as in the t-driven equation, while avoiding the explicit pre-calculation and interpolation of the fully off-shell two-body t-matrix. Depending on the grid sizes and interpolation strategy, this formulation may also reduce the computational cost [33].

While Eq. (36) allows the use of the full bare interaction directly, validating the 3D approach against the 1D and 2D methods requires a strict one-to-one comparison. With the partial-wave normalization used in Secs. III and IV, the interaction can be expanded as

$$V(p,p',\hat{\mathbf{p}}\cdot\hat{\mathbf{p}}') = \sum_l \frac{2l+1}{4\pi} P_l(\hat{\mathbf{p}}\cdot\hat{\mathbf{p}}')\, V_l(p,p')\,. \quad (41)$$

Inserting this expansion into the azimuthal integration and using the standard azimuthal projection identity yields

$$v(p,p',x,x') = \sum_l \frac{2l+1}{4\pi} V_l(p,p') \int_0^{2\pi} d\varphi'\, P_l(y) = \sum_l \frac{2l+1}{2} V_l(p,p')\, P_l(x)\, P_l(x')\,, \quad (42)$$

which allows the same finite partial-wave interaction space to be embedded directly into the 3D vector formulation.

The full three-boson wave function is constructed via Eq. (4). For the spinless bosonic state considered here, $\Psi(\mathbf{p},\mathbf{q}) = \Psi(-\mathbf{p},\mathbf{q})$. Mapping the internal vector angles, the full wave function can be compactly written as

$$\Psi(p,q,x) = \psi(p,q,x) + \psi(\tilde{\pi}_1^+,\tilde{\pi}_2^+,x^+) + \psi(\tilde{\pi}_1^-,\tilde{\pi}_2^-,x^-), \tag{43}$$

where the shifted momentum magnitudes for the cyclic (+) and anticyclic (−) permutations are given by

$$\tilde{\pi}_1^\pm = \sqrt{\tfrac{1}{4}p^2 + \tfrac{9}{16}q^2 \pm \tfrac{3}{4}pqx}$$
$$\tilde{\pi}_2^\pm = \sqrt{p^2 + \tfrac{1}{4}q^2 \mp pqx}. \tag{44}$$

Notice that the positive branches, $\tilde{\pi}_1^+$ and $\tilde{\pi}_2^+$, are precisely the shifted variables $\tilde{\pi}_1$ and $\tilde{\pi}_2$ defined in Eq. (23) for the partial-wave recoupling.

The corresponding internal angular arguments are determined by the scalar products of the shifted vectors

$$x^\pm = \frac{\pm\left(\frac{3}{8}q^2 - \frac{1}{2}p^2\right) - \frac{1}{2}pqx}{\tilde{\pi}_1^\pm\,\tilde{\pi}_2^\pm}. \tag{45}$$

This compact notation shows that the permutation geometry used in the 3D continuous-variable representation is the same geometry that underlies the shifted arguments in the coupled partial-wave representation.

The full three-body wave function is normalized according to

$$1 = \langle\Psi|\Psi\rangle = 8\pi^2 \int_0^\infty dp\, p^2 \int_0^\infty dq\, q^2 \int_{-1}^1 dx\, |\Psi(p,q,x)|^2 \tag{46}$$

$$= 3\langle\psi|\Psi\rangle = 24\pi^2 \int_0^\infty dp\, p^2 \int_0^\infty dq\, q^2 \int_{-1}^1 dx\, \psi^*(p,q,x)\,\Psi(p,q,x)\,. \tag{47}$$

In the exact continuous limit, both integral forms must yield identical results. In our discretized 3D vector approach, computing both forms provides a stringent numerical consistency check.

The full Hamiltonian expectation value is evaluated as

$$\langle H\rangle = 3\langle\psi|H_0|\Psi\rangle + 3\langle\Psi|V_1|\Psi\rangle. \tag{48}$$

The reduced kinetic-energy matrix element is

$$\langle\psi|H_0|\Psi\rangle = 8\pi^2 \int_0^\infty dp\, p^2 \int_0^\infty dq\, q^2 \left(p^2 + \frac{3}{4}q^2\right) \times \int_{-1}^1 dx\, \psi^*(p,q,x)\,\Psi(p,q,x), \tag{49}$$

and the matrix element of one pair interaction is

$$\langle\Psi|V_1|\Psi\rangle = 8\pi^2 \int_0^\infty dp\, p^2 \int_0^\infty dq\, q^2 \int_0^\infty dp'\, p'^2 \int_{-1}^1 dx \int_{-1}^1 dx' \times \Psi^*(p,q,x)\, v(p,p',x,x')\,\Psi(p',q,x')\,, \tag{50}$$

where the azimuthal dependence has already been absorbed into the azimuthally integrated potential v defined in Eq. (36), or into its truncated partial-wave representation defined in Eq. (42).

The full wave function $\Psi(\mathbf{p},\mathbf{q})$ can be expanded in terms of partial-wave components $\Psi_l(p,q)$

$$\Psi(\mathbf{p},\mathbf{q}) = \Psi(p,q,x) = \sum_l \frac{\sqrt{2l+1}}{4\pi}\,P_l(x)\,\Psi_l(p,q). \tag{51}$$

Conversely, the partial-wave components are obtained by projecting the 3D solutions onto the Legendre polynomials

$$\Psi_l(p,q) = 2\pi\sqrt{2l+1}\int_{-1}^1 dx\, P_l(x)\,\Psi(p,q,x). \tag{52}$$

These relations allow for a direct numerical mapping between the 3D vector-variable results and the converged partial-wave expansions used in the 1D and 2D approaches, facilitating the benchmark comparisons presented in Sec. IX.

VI. OBSERVABLES AND WAVE FUNCTION ANALYSIS

In physical applications, the multidimensional wave function is usually analyzed through expectation values and reduced distributions. For instance, the spectator momentum distribution $n_{\rm spec}(q)$ represents the probability of finding a boson with momentum q relative to the center of mass of the interacting pair. Complementarily, the subsystem momentum distribution $n_{\rm sub}(p)$ represents the internal momentum of that pair. Using the full 3D wave function and the partial-wave components, these distributions are evaluated as

$$n_{\rm spec}(q) = 2\pi q^2 \int_0^\infty dp\, p^2 \int_{-1}^1 dx\, |\Psi(p,q,x)|^2 = \frac{q^2}{4\pi}\sum_l \int_0^\infty dp\, p^2\, |\Psi_l(p,q)|^2, \tag{53}$$

$$n_{\rm sub}(p) = 2\pi p^2 \int_0^\infty dq\, q^2 \int_{-1}^1 dx\, |\Psi(p,q,x)|^2 = \frac{p^2}{4\pi}\sum_l \int_0^\infty dq\, q^2\, |\Psi_l(p,q)|^2, \tag{54}$$

where x generally denotes the cosine of the angle between the relevant Jacobi vectors. With this convention, the remaining solid-angle factor is kept outside the definition of

the radial distributions, so that $4\pi \int_0^\infty dq\, n_{\rm spec}(q) = 1$ and $4\pi \int_0^\infty dp\, n_{\rm sub}(p) = 1$. By comparing the partial-wave sums to the corresponding 3D vector integrals, we can quantify the angular momentum content required to saturate the state within the chosen numerical accuracy.

A. Coordinate-Space Transformation: 3D Vector Approach

To investigate the spatial structure of the bound state, we transform the momentum-space wave function $\Psi(\mathbf{p}, \mathbf{q})$ into configuration space. We define the conjugate spatial Jacobi coordinates $\mathbf{r}$ (the two-body subsystem distance) and $\boldsymbol{\rho}$ (the distance of the third particle to the pair's center of mass).

For the 3D vector-variable approach, we perform the unitary transformation without introducing a partial-wave expansion. The full double Fourier integral is given by

$$\tilde{\Psi}(\mathbf{r}, \boldsymbol{\rho}) = \frac{1}{(2\pi)^3} \int d^3p \int d^3q\, \Psi(\mathbf{p}, \mathbf{q})\, e^{i\mathbf{p}\cdot\mathbf{r}}\, e^{i\mathbf{q}\cdot\boldsymbol{\rho}}. \quad (55)$$

We evaluate this in two steps to preserve numerical stability [34]. First, we transform the spectator momentum $\mathbf{q}$ to $\boldsymbol{\rho}$

$$I_q(\mathbf{p}, \boldsymbol{\rho}) = \frac{1}{(2\pi)^{3/2}} \int d^3q\, \Psi(\mathbf{p}, \mathbf{q})\, e^{i\mathbf{q}\cdot\boldsymbol{\rho}}. \quad (56)$$

Choosing $\mathbf{p} \parallel \hat{z}$, we define the internal angles $x_q = \hat{\mathbf{q}} \cdot \hat{\mathbf{p}}$ and $\mu = \hat{\boldsymbol{\rho}} \cdot \hat{\mathbf{p}}$. The azimuthal integration over ϕ_q reduces the angular dependence to a zeroth-order cylindrical Bessel function J_0. For the real bound-state wave functions considered here, the imaginary part of the Fourier integral vanishes by symmetry. We therefore retain only the real part, which after the azimuthal integration is

$$I_q(p, \rho, \mu) = \frac{1}{\sqrt{2\pi}} \int_0^\infty dq\, q^2 \int_{-1}^{1} dx_q\, \cos(q\rho x_q \mu) \times J_0\left(q\rho\sqrt{1-x_q^2}\,\sqrt{1-\mu^2}\right) \Psi(p, q, x_q). \quad (57)$$

Parseval's theorem for this $q \to \rho$ transformation yields the partial unitarity identity

$$8\pi^2 \int_0^\infty dp\, p^2 \int_0^\infty d\rho\, \rho^2 \int_{-1}^{1} d\mu\, |I_q(p, \rho, \mu)|^2 = 1, \quad (58)$$

which provides a stringent numerical consistency check for the intermediate projection prior to the final spatial integration.

The second step completes the transformation into full coordinate space

$$\tilde{\Psi}(\mathbf{r}, \boldsymbol{\rho}) = \frac{1}{(2\pi)^{3/2}} \int d^3p\, I_q(\mathbf{p}, \boldsymbol{\rho})\, e^{i\mathbf{p}\cdot\mathbf{r}}. \quad (59)$$

Choosing $\mathbf{r} \parallel \hat{z}$ and defining the spatial angles $x_p = \hat{\mathbf{p}} \cdot \hat{\mathbf{r}}$ and $x_r = \hat{\boldsymbol{\rho}} \cdot \hat{\mathbf{r}}$, the internal angular coupling becomes $\mu = x_p x_r + \sqrt{1-x_p^2}\,\sqrt{1-x_r^2}\,\cos\phi_p$.

An angular reduction of the final p-integration to a spherical Bessel factor would be valid only if the remaining integrand were independent of the direction of $\mathbf{p}$. In the present two-step transformation this condition is not satisfied. After the $q \to \rho$ transformation, the intermediate amplitude I_q depends on the angle $\mu = \hat{\boldsymbol{\rho}} \cdot \hat{\mathbf{p}}$. During the subsequent integration over the direction of $\mathbf{p}$, this angle varies according to

$$\mu = x_p x_r + \sqrt{1-x_p^2}\sqrt{1-x_r^2}\cos\phi_p. \quad (60)$$

Thus $I_q(p, \rho, \mu)$ cannot be taken outside the angular integration over $\mathbf{p}$, and the full azimuthal integral over ϕ_p must be retained. For the same symmetry reasons noted above, only the real part of the final Fourier integral contributes

$$\tilde{\Psi}(r, \rho, x_r) = \frac{1}{(2\pi)^{3/2}} \int_0^\infty dp\, p^2 \int_{-1}^{1} dx_p \int_0^{2\pi} d\phi_p \times \cos(prx_p)\, I_q(p, \rho, \mu). \quad (61)$$

In the continuous limit, this formulation exactly preserves the norm of Eq. (46); computational deviations from this identity provide a useful measure of the numerical accuracy of the spatial transformation.

B. Coordinate-Space Transformation: Partial-Wave Approach

For a bound state with zero total angular momentum ($\mathcal{L} = 0$), we insert the Legendre expansion of the momentum-space wave function, given in Eq. (51), into the unitary transformation of Eq. (55). Expanding the plane waves into spherical harmonics and spherical Bessel functions $j_l(z)$, and applying the spherical harmonic addition theorem, the angular integrations decouple completely.

Using the orthogonality of the spherical harmonics and collecting the phases, the spatial wave function takes the partial-wave form

$$\tilde{\Psi}(\mathbf{r}, \boldsymbol{\rho}) = \sum_l \frac{\sqrt{2l+1}}{4\pi} P_l(\hat{\mathbf{r}} \cdot \hat{\boldsymbol{\rho}})\, \tilde{\Psi}_l(r, \rho), \quad (62)$$

where the radial components $\tilde{\Psi}_l(r, \rho)$ are given by the double spherical Bessel transform

$$\tilde{\Psi}_l(r, \rho) = \frac{2}{\pi}(-1)^l \times \int_0^\infty dp\, p^2 j_l(pr) \int_0^\infty dq\, q^2 j_l(q\rho)\, \Psi_l(p, q). \quad (63)$$

Because the angular integrations have been performed analytically, this representation avoids the azimuthal coupling inherent to the direct 3D transform, requiring only the evaluation of the oscillatory radial integrals.

C. Spatial Geometry and Observables

Using this spatial representation, the radial correlation function $c_{\rm sub}(r)$ describes the distribution of separations r between the two subsystem bosons. Similarly, $c_{\rm spec}(\rho)$ describes the distribution of distances ρ between the third boson and the subsystem center of mass. In terms of the full 3D state and the partial-wave components, these are evaluated as

$$c_{\rm sub}(r) = 2\pi r^2 \int_0^\infty d\rho\, \rho^2 \int_{-1}^{1} dx_r\, |\tilde{\Psi}(r,\rho,x_r)|^2 = \frac{r^2}{4\pi} \sum_l \int_0^\infty d\rho\, \rho^2\, |\tilde{\Psi}_l(r,\rho)|^2, \tag{64}$$

$$c_{\rm spec}(\rho) = 2\pi \rho^2 \int_0^\infty dr\, r^2 \int_{-1}^{1} dx_r\, |\tilde{\Psi}(r,\rho,x_r)|^2 = \frac{\rho^2}{4\pi} \sum_l \int_0^\infty dr\, r^2\, |\tilde{\Psi}_l(r,\rho)|^2. \tag{65}$$

As for the momentum distributions, the remaining solid-angle factor is kept outside the definition of the radial distributions. Thus $4\pi \int_0^\infty dr\, c_{\rm sub}(r) = 1$ and $4\pi \int_0^\infty d\rho\, c_{\rm spec}(\rho) = 1$.

A symmetric spatial configuration of three identical bosons can be geometrically compared to an equilateral triangle. The expectation values of the spatial Jacobi coordinates represent the base length $\langle r\rangle$ and the height $\langle \rho\rangle$ of this triangle

$$\langle r\rangle = 8\pi^2 \int_0^\infty d\rho\, \rho^2 \int_0^\infty dr\, r^3 \int_{-1}^{1} dx_r\, |\tilde{\Psi}(r,\rho,x_r)|^2 = \sum_l \int_0^\infty d\rho\, \rho^2 \int_0^\infty dr\, r^3\, |\tilde{\Psi}_l(r,\rho)|^2, \tag{66}$$

$$\langle \rho\rangle = 8\pi^2 \int_0^\infty d\rho\, \rho^3 \int_0^\infty dr\, r^2 \int_{-1}^{1} dx_r\, |\tilde{\Psi}(r,\rho,x_r)|^2 = \sum_l \int_0^\infty dr\, r^2 \int_0^\infty d\rho\, \rho^3\, |\tilde{\Psi}_l(r,\rho)|^2. \tag{67}$$

Equivalently, the same expectation values follow from the radial correlation functions,

$$\langle r\rangle = 4\pi \int_0^\infty dr\, r\, c_{\rm sub}(r), \qquad \langle \rho\rangle = 4\pi \int_0^\infty d\rho\, \rho\, c_{\rm spec}(\rho). \tag{68}$$

For a single equilateral configuration, the ratio between the base and height is $r/\rho = 2/\sqrt{3}$. The quantum bound state does not impose this relation pointwise on the probability distribution. Nevertheless, the ratio $\langle r\rangle/\langle\rho\rangle$ provides a useful diagnostic of the average spatial correlations. We therefore define the deviation from the equilateral reference value as

$$\delta = \frac{\langle r\rangle/\langle\rho\rangle - 2/\sqrt{3}}{2/\sqrt{3}} \times 100. \tag{69}$$

Evaluating these spatial integrals provides a compact measure of how the average geometry depends on the underlying interaction.

VII. TWO-BODY INTERACTIONS

For the separable interactions introduced in Sec. III, we employ generalized Yamaguchi form factors defined for all partial waves as

$$g_l(p) = \frac{p^l}{(p^2+\beta^2)^{l+1}}\,. \tag{70}$$

For $l = 0$, this reduces to the original Yamaguchi form factor [26]. With the Fourier–Bessel convention used in this work, the corresponding $l = 0$ coordinate-space form factor is

$$\tilde{g}_0(r) = \sqrt{\frac{\pi}{2}}\,\frac{e^{-\beta r}}{r}\,. \tag{71}$$

Although the calculations are performed in momentum space, the coordinate-space representation provides useful checks for spatial observables and potential-energy expectation values. Exact analytical spatial representations can also be derived for higher partial waves ($l > 0$), but the resulting polynomial structures become increasingly cumbersome. In the literature, several parameter sets are used for the Yamaguchi potential, often together with slightly different conversion conventions. Table I lists the parameter sets considered here, the conversion factors employed, and the exact s-wave two-body binding energy E_2 obtained analytically [35].

As a second class of interaction models, we employ local Malfliet–Tjon (MT) potentials of Yukawa type [27, 36]. While these central interactions do not include tensor components or spin dependence, they provide useful benchmark potentials with simple analytic momentum-space representations. Depending on the parameter set, they also include a finite short-range repulsive component and therefore test the convergence of the high-momentum part of the wave function. In coordinate space, they are given by

$$\tilde{V}(r) = V_a\,\frac{e^{-\mu_a r}}{r} + V_r\,\frac{e^{-\mu_r r}}{r}\,, \tag{72}$$

where the long-range attractive part is characterized by V_a and μ_a, and the short-range repulsive part by V_r and μ_r. In the parameter sets used below, $V_a < 0$ and $V_r \geq 0$.

TABLE I. Parameters and conversion factors for the Yamaguchi potentials. The resulting two-body binding energies E_2 have been calculated analytically [35]. Listed values are the exact ones used in calculations.

Potential	β [fm^{-1}]	λ [fm^{-3}]	$(\hbar c)^2/m_N$ [MeV fm^2]	$\hbar c$ [MeV fm]	E_2 [MeV]	Ref.
YAMA-23	1.3905818	0.3707654	41.47103997	197.3269804	−2.22456720	[35]
YAMA-IV	1.15	0.179	41.47	197.3286	−0.33178133	[14]

TABLE II. Parameters for the Malfliet–Tjon potentials and conversion factors from the cited references. The resulting two-body binding energies E_2 have been calculated in [35]. Listed values are the exact ones used in calculations.

Potential	V_a [MeV fm]	μ_a [fm^{-1}]	V_r [MeV fm]	μ_r [fm^{-1}]	$(\hbar c)^2/m_N$ [MeV fm^2]	$\hbar c$ [MeV fm]	E_2 [MeV]	Ref.
MT-IV	−65.109	0.633	–	–	41.47	197.3	−2.20862918	[4]
MT-V	−570.3316	1.55	1438.4812	3.11	41.47	197.3	−0.35000049	[4]

With the momentum-space normalization used in this work, the partial-wave matrix elements take the closed form

$$V_l(p,p') = \frac{1}{\pi p p'} \left[V_a\, Q_l(z_a) + V_r\, Q_l(z_r) \right] , \tag{73}$$

with

$$z_{a/r} = \frac{p^2 + p'^2 + \mu_{a/r}^2}{2pp'} , \tag{74}$$

where $Q_l(z)$ denotes the Legendre function of the second kind. For regular central potentials in this normalization, the partial-wave matrix elements with $l > 0$ vanish when either external momentum approaches zero. For numerical use near the grid boundaries, the $l = 0$ matrix element is evaluated through its finite boundary form

$$V_0(p,p')\Big|_{p=0 \text{ or } p'=0} = \frac{2}{\pi} \left(\frac{V_a}{p^2 + p'^2 + \mu_a^2} + \frac{V_r}{p^2 + p'^2 + \mu_r^2} \right) . \tag{75}$$

With this normalization, the full vector-variable matrix element is related to the partial-wave matrix elements through the expansion introduced in Sec. V. It is given by

$$V(\mathbf{p},\mathbf{p}') = \frac{1}{2\pi^2} \left[\frac{V_a}{(\mathbf{p}-\mathbf{p}')^2 + \mu_a^2} + \frac{V_r}{(\mathbf{p}-\mathbf{p}')^2 + \mu_r^2} \right] . \tag{76}$$

With the definition of v as the full azimuthal integral in Eq. (36), this integration can be performed analytically. Writing x and x' as the cosines of the polar angles entering Eq. (36), the resulting azimuthally integrated interaction $v(p,p',x,x')$, used directly in the 3D integral kernels, is explicitly given by

$$v(p,p',x,x') = \frac{1}{\pi} \left[\frac{V_a}{\sqrt{\left(p^2 + p'^2 - 2\,p\,p'\,x\,x' + \mu_a^2\right)^2 - 4\,p^2\,p'^2(1-x^2)(1-x'^2)}} + \frac{V_r}{\sqrt{\left(p^2 + p'^2 - 2\,p\,p'\,x\,x' + \mu_r^2\right)^2 - 4\,p^2\,p'^2(1-x^2)(1-x'^2)}} \right] . \tag{77}$$

Table II collects the parameter sets adopted here and the corresponding conversion factors.

VIII. NUMERICAL METHODS

The numerical strategy closely follows the approach established in the two-body study [35], extended here to the higher-dimensional three-body kernels. The determination of the three-body bound-state energy and wave function in momentum space requires the solution of the homogeneous

Faddeev equations at negative energies. For a fixed trial energy E, the discretized equation is written as an eigenvalue problem for the kernel $K(E)$

$$K(E)|\psi\rangle = \eta(E)|\psi\rangle. \tag{78}$$

The physical three-body binding energy E_3 is determined by the condition

$$\eta(E_3) = 1. \tag{79}$$

For each trial energy, the two-body input is constructed either as a fully off-shell t-matrix or directly from the potential matrix elements, depending on whether the t-driven or V-driven formulation is used. The resulting three-body kernel is applied to a trial Faddeev component on the discretized momentum and angular grids. A Krylov subspace method [37, 38] is then used to determine the eigenvalue associated with the physical bound-state branch. The total energy E is varied until the condition $\eta(E_3) = 1$ is fulfilled. After convergence, the Faddeev component is used to reconstruct the full wave function, normalize the state, evaluate expectation values, and, where required, transform the momentum-space wave function into coordinate space.

A. Discretization and Iteration

All continuous momentum and angular variables are discretized using Gauss–Legendre quadrature rules. The semi-infinite momentum intervals are truncated at finite cutoffs $p_{\max}$ and $q_{\max}$. As detailed in the convergence studies below, evaluating the Hamiltonian expectation values requires significantly larger cutoffs than determining the binding energies alone. For the production calculations reported below, we use a spectator momentum cutoff of $q_{\max} = 400$ fm^{-1} for the separable Yamaguchi interactions. Due to the shifted momentum arguments in the permutation operator, the corresponding internal momentum cutoff is strictly bounded by $p_{\max} = \frac{3}{2}q_{\max} = 600$ fm^{-1}. For the local Malfliet–Tjon potentials, $q_{\max} = 200$ fm^{-1} ($p_{\max} = 300$ fm^{-1}) is sufficient at the quoted accuracy.

To obtain a dense grid in the physically dominant low-momentum region, the momentum intervals are divided into subintervals, $(0, p_0) \cup (p_0, p_{\max})$ and $(0, q_0) \cup (q_0, q_{\max})$, with representative boundary values $p_0 = 9$ fm^{-1} and $q_0 = 10$ fm^{-1}. The mappings described in Ref. [39] are used to distribute the quadrature points efficiently. Here N_p and N_q denote the total number of quadrature points over both momentum subintervals. While 128 momentum points are sufficient for the binding energies at the accuracy discussed below, resolving the expectation values to the 10^{-5} MeV level requires substantially denser grids of $N_p = N_q = 384$–768 points.

For the angular variables, Gauss–Legendre quadrature is employed with $N_x = 34$–50 points for $x = \hat{\mathbf{p}} \cdot \hat{\mathbf{q}}$. In the 3D vector-variable formulation, the azimuthal angle is additionally discretized with $N_\varphi \simeq 24$ points. The boundary points $p = 0$, $q = 0$, and $x = \pm 1$ are explicitly included in the numerical grids with zero quadrature weight. These points do not contribute to the quadrature sums, but are available for interpolation and exact function evaluations at kinematic boundaries, thereby avoiding numerical extrapolation.

The permutation operator introduces shifted momenta, such as (π_1, π_2), which generally do not coincide with the quadrature points. Consequently, the evaluation of the integral kernels requires interpolation of the wave functions and, in the t-driven formulations, of the fully off-shell two-body t-matrix. We employ local cubic Hermite splines [32] for interpolation in the continuous momentum and angular variables required by the shifted arguments. This interpolation provides a stable representation of the off-shell t-matrix and Faddeev amplitudes while avoiding the Runge oscillations typical of high-order global polynomial interpolation [29].

For the 1D separable formulation, the discretized equation leads to a matrix eigenvalue problem of moderate size that can be solved by standard direct methods. In the 2D and 3D formulations, the dimension of the discretized state vector is much larger, typically $N \sim 10^5$–10^6. Explicit construction and storage of the full kernel matrix $K(E)$ is therefore impractical. Instead, the equation is solved iteratively by computing only the action of the kernel on a trial vector,

$$|v'\rangle = K(E)|v\rangle. \tag{80}$$

This matrix-free operation defines the Krylov subspace used to extract the relevant eigenvalues.

As a check on numerical robustness, two independent eigensolvers are implemented. The first is a custom subspace projection method based on Ref. [38]. It constructs an orthogonal basis by repeated kernel applications, explicitly initialized with a smooth analytic trial function $\psi(p, q, x) \sim [(0.5 + p^2)(0.5 + q^2)]^{-1}$, and diagonalizes the resulting small Rayleigh–Ritz matrix.

The second, primary solver utilizes the implicitly restarted Arnoldi method [37] provided by the ARPACK library. Operating via a reverse-communication interface, this method automatically builds the Krylov subspace using only matrix-vector products, without requiring a prescribed analytic starting vector. To ensure that the physical bound state is reliably identified and continuously tracked across successive trial energy updates, a wavefunction overlap tracking algorithm (root homing) is employed. For all calculations reported below, the eigensolver iterations are terminated when the relative change of the eigenvalue falls below 10^{-10}.

Because the evaluation of the kernel action is computationally demanding, the multidimensional integrations are heavily parallelized using the Message Passing Interface (MPI). The spectator momentum grid q is distributed across MPI ranks, and the resulting partial integrals are combined via global reductions at each iteration step.

Since the kernel depends nonlinearly on the total energy E, the eigenvalue problem must be solved repeatedly to determine the physical energy E_3. This is done using an outer root-finding procedure. Starting from two initial energy values, a stabilized secant iteration is used to dynamically update the energy. The iteration is stopped when both $|\eta(E) - 1|$ and the change in E fall below the prescribed tolerances (typically 10^{-10} and 10^{-8} MeV, respectively).

B. Numerical Evaluation of Spatial Observables

The unitary transformation of the momentum-space wave functions into coordinate space introduces significant numerical challenges due to oscillatory integrands and finite-domain truncation errors. To transform the 3D vector-variable wave function into coordinate space, we employ two complementary procedures. In the first, the 3D momentum-space wave function is projected onto partial waves and transformed using the double spherical Bessel transform, mimicking the native 2D formulation. In the second, the vector-variable Fourier transform is evaluated directly after the analytical angular reductions described in Sec. VI, without expanding the wave function in partial waves. Agreement between the two procedures provides a sensitive internal consistency check.

The partial-wave transformation relies on integrating the momentum-space wave functions against spherical Bessel functions $j_l(pr)$ and $j_l(q\rho)$. Because these functions oscillate rapidly at large spatial distances and high momenta, the momentum grids must resolve the relevant oscillation scales. In the calculations reported here, the sums are carried out up to $l_{\max} = 12$. For these angular momenta, standard upward recurrence relations for the spherical Bessel functions remain numerically stable.

For the direct vector-variable transformation, the intermediate $q \to \rho$ projection contains the cylindrical Bessel function J_0. Evaluating this integral directly on the original angular grid can lead to aliasing errors in the oscillatory kernel. To suppress this error, the wave function $\Psi(p, q, x_q)$ is first interpolated onto a dense 256-point Gauss–Legendre mesh in x_q, which provides a more accurate resolution of the Bessel oscillations.

For the final $p \to r$ projection, standard Gaussian quadrature is again inefficient for the highly oscillatory $\cos(prx_p)$ kernel. We therefore employ a hybrid Filon quadrature scheme [28, 29]. The smooth momentum-space envelope is spline-interpolated, while the trigonometric factor is integrated analytically over fine subintervals. For $pr < 0.1$, where the analytical Filon weights are susceptible to floating-point cancellation, the algorithm automatically switches to a stabilized high-density trapezoidal rule using a locally refined mesh. In the calculations reported below, this hybrid integration typically preserves the Fourier-transform norm at the level of $O(10^{-4})$.

To evaluate the kinetic-energy expectation value in coordinate space, we use the mixed Faddeev overlap for the full kinetic energy,

$$\langle H_0 \rangle = 3\langle \psi | H_0 | \Psi \rangle. \tag{81}$$

With the Jacobi convention used here, the coordinate-space kinetic operator is $H_0 = -\nabla_r^2 - \frac{3}{4}\nabla_\rho^2$. Applying the second-derivative Laplacian operator directly to numerically transformed coordinate-space wave functions is prone to instability, as finite momentum cutoffs produce oscillatory ringing near the spatial origin. We avoid this by utilizing integration by parts to recast the kinetic-energy matrix element entirely in terms of first spatial derivatives.

Rather than computing these gradients via finite differences on the spatial mesh, the radial derivatives $\partial/\partial r$ and $\partial/\partial\rho$ are evaluated analytically during the momentum-space transformations. By substituting the spherical Bessel functions $j_l(kx)$ with their exact analytical derivatives $k\, j_l'(kx)$ within the integration kernels, first-derivative wave functions based on the analytical kernel derivatives are generated concurrently with the standard spatial wave functions. This approach eliminates numerical differentiation artifacts and yields a highly stable coordinate-space evaluation of $\langle H_0 \rangle$.

Finally, the evaluation of the potential-energy expectation value in coordinate space depends on the nature of the interaction. For local interactions, such as the Malfliet–Tjon potential, $\langle V \rangle$ is evaluated by integrating the coordinate-space potential $\tilde{V}(r)$ over the coordinate-space probability density. Conversely, for separable interactions such as the Yamaguchi potential, the coordinate-space potential is represented through the nonlocal separable kernel constructed from the spatial form factors $\tilde{g}_l(r)$. Because the corresponding momentum-space form factors $g_l(p)$ decay slowly at high momenta, their Fourier transforms are highly susceptible to truncation artifacts. To suppress these artifacts, the spatial form factors $\tilde{g}_l(r)$ for $l > 0$ are evaluated using Filon quadrature. This semi-analytical integration scheme explicitly accounts for the rapid oscillations of the spherical Bessel functions, allowing us to accurately integrate over an independent, high-density momentum grid extending to $p = 5000$ fm^{-1}. For the s-wave, numerical integration is bypassed entirely in favor of the exact analytical representation of Eq. (71).

IX. RESULTS AND DISCUSSION

A. Baseline Validation: Separable Interactions

As a first benchmark, we consider three identical bosons interacting through rank-one separable Yamaguchi potentials. In this case, the two-body t-matrix is known analytically, and the Faddeev equations reduce to coupled one-dimensional integral equations for the spectator amplitudes $F_l(q)$. The 1D calculation therefore provides a high-precision reference against which the higher-dimensional formulations are tested.

Figure 1 shows the corresponding spectator amplitudes $|F_l(q)|$ for the YAMA-23 potential evaluated in both double and quadruple precision. While the dominant partial waves are perfectly stable, the double-precision calculation exhibits visible numerical noise near the origin for the highly suppressed $l = 10$ and $l = 12$ channels, where the amplitudes drop into the 10^{-20} to 10^{-25} range. As shown in the right panel, elevating the calculation to quadruple precision removes the visible round-off noise, restoring the smooth behavior of the amplitudes down to the lowest momenta, while also providing a slight correction to the $l = 8$ channel. This comparison indicates that the underlying integral equations remain well-conditioned, and that the observed noise is a finite-precision artifact.

A notable numerical feature of the one-dimensional approach is the large difference between the effort required to determine the eigenvalue energy and that required to evaluate expectation values from the reconstructed full wave function. As detailed in Appendix A (Table XIV), the eigenvalue energy obtained

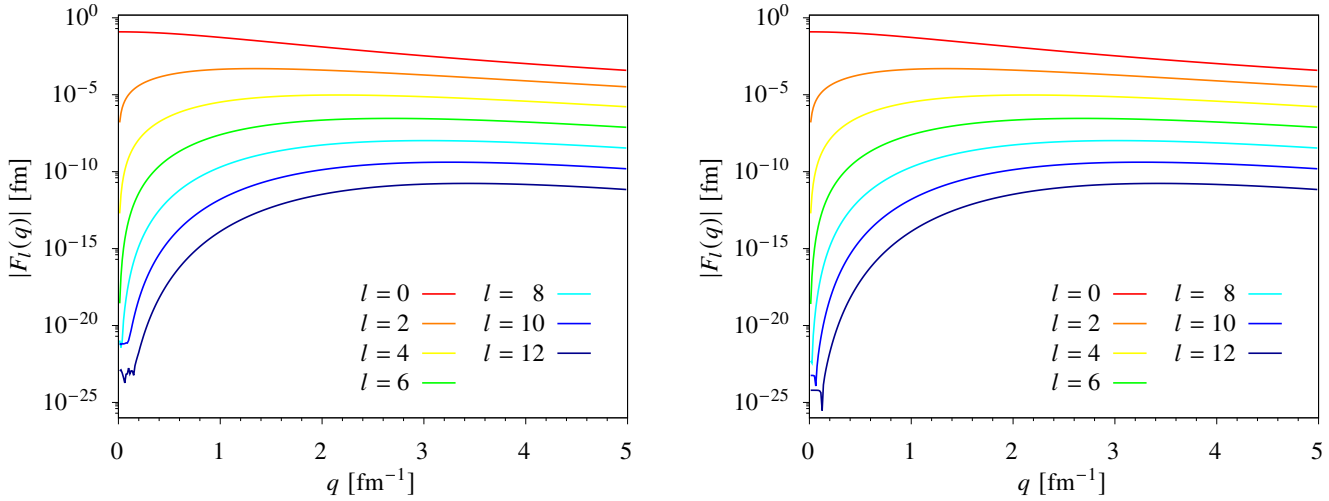


FIG. 1. Three-boson spectator amplitudes $|F_l(q)|$ for the YAMA-23 potential with partial waves $l = 0, 2, 4, 6, 8, 10, 12$. The left panel shows the double-precision calculation, while the right panel shows the corresponding quadruple-precision calculation.

from Eq. (17) converges very rapidly. For the YAMA-23 potential at $l_{\max} = 12$, a cutoff of $q_{\rm cut} = 30$ fm^{-1} with $N = 48$ Gauss–Legendre points is already sufficient to stabilize E_3 at the displayed precision.

The expectation values are considerably more demanding. Their evaluation requires the reconstructed wave function $\Psi_l(p, q)$ over the two-dimensional momentum domain. In particular, the kinetic-energy operator $p^2 + \frac{3}{4}q^2$, together with the integration measure $p^2 dp\, q^2 dq$, strongly enhances the high-momentum tail. Consequently, a much larger cutoff is needed to obtain the same internal consistency in $\langle H \rangle$. Appendix A (Table XIII) shows that $\Delta E = |E_3 - \langle H \rangle|$ falls below 10^{-5} MeV only once the cutoff reaches about $q_{\rm cut} = 200$ fm^{-1}, and is reduced to 9×10^{-7} MeV at $q_{\rm cut} = 400$ fm^{-1}.

Having established the necessary momentum boundary, we next determine the required grid density. Table XV in Appendix A shows the convergence of the expectation values with respect to the number of grid points N, evaluated at a fixed, sufficient cutoff of $q_{\rm cut} = 400$ fm^{-1}. While $N = 128$ already gives a useful estimate, suppressing the internal residual ΔE below 10^{-5} MeV requires dense integration grids of $N \geq 384$. This stiffness illustrates the numerical demands imposed by the three-body geometry and foreshadows the more demanding convergence behavior encountered for the local Malfliet–Tjon potentials.

A strict comparison between the 1D, 2D, and 3D calculations requires that all formulations be evaluated in the same truncated partial-wave interaction space. For this reason, the truncated partial-wave interaction is embedded directly into the 2D and 3D kernels using Eq. (42). Thus, differences between the calculated binding energies can be attributed to discretization, interpolation, and permutation geometry, rather than to different model spaces.

Table III shows the convergence of the three-body binding energies and expectation values for the YAMA-23 and YAMA-IV potentials as a function of the included two-body angular momentum $l_{\max}$, establishing the final 1D baseline. The partial-wave expansion converges rapidly; for both potentials, the change between $l_{\max} = 4$ and $l_{\max} = 6$ is negligible at the displayed precision. To ensure a strict comparison with the 2D and 3D calculations presented in subsequent sections, the 1D momentum grid is chosen to match the high-density 2D grids ($q_{\rm cut} = 400$ fm^{-1}, $p_{\rm cut} = 600$ fm^{-1}, $N_p = N_q = 768$).

The saturated 1D results can now be compared directly with the independently implemented 2D partial-wave formulation in Table IV and the 3D vector-variable formulation in Table V. For YAMA-23, the corresponding binding energies are

$$\begin{aligned} E_3^{\rm 1D} &= -24.5385691 \text{ MeV}, \\ E_3^{\rm 2D} &= -24.5385697 \text{ MeV}, \\ E_3^{\rm 3D} &= -24.5385697 \text{ MeV}, \end{aligned} \tag{82}$$

showing agreement at the 10^{-6} MeV level. The individual expectation values $\langle H_0 \rangle$ and $\langle V \rangle$ are more sensitive to high-momentum tails, interpolation, and multidimensional quadrature, and therefore agree at the 10^{-5}–10^{-4} MeV level. Their sum $\langle H \rangle$, however, remains consistent with the eigenvalue energy at the few-10^{-6} MeV level. Consistent with the 1D baseline, the 2D calculations are performed with $q_{\rm cut} = 400$ fm^{-1} ($p_{\rm cut} = 600$ fm^{-1}) using $N_p = N_q = 768$ mesh points. The 3D calculations employ a slightly reduced momentum grid, $N_p = N_q = 512$, together with $N_x = 34$, due to the added azimuthal dimensionality. A similar precision is obtained for YAMA-IV.

The residual $|E_3 - \langle H \rangle|$ provides an independent internal check of the reconstructed wave functions. For the final Yamaguchi calculations, the residuals are at the 10^{-6} MeV level in all three formulations, with the 3D calculation reaching 3.0×10^{-6} MeV for YAMA-23 and 4×10^{-7} MeV for YAMA-IV at the largest displayed partial-wave truncation.

The angular content of the calculated wave functions is further tested by decomposing the total norm into individual

TABLE III. Expectation values $\langle H\rangle$, $\langle H_0\rangle$, $\langle V\rangle$, and three-body binding energy E_3 for the Yamaguchi potentials within the 1D approach, shown as a function of the maximum two-body angular momentum $l_{\max}$, with $q_{\rm cut} = 400$ fm^{-1} ($p_{\rm cut} = 600$ fm^{-1}) and $N_p = N_q = 768$ points.

Potential	$l_{\max}$	$\langle H_0\rangle$ [MeV]	$\langle V\rangle$ [MeV]	$\langle H\rangle$ [MeV]	E_3 [MeV]	$\lvert E_3 - \langle H\rangle\rvert$ [MeV]
YAMA-23	0	67.1444332	−91.6723094	−24.5278762	−24.5278771	0.0000009
YAMA-23	2	67.1493091	−91.6878677	−24.5385586	−24.5385595	0.0000009
YAMA-23	4	67.1492968	−91.6878650	−24.5385682	−24.5385691	0.0000009
YAMA-23	6	67.1492967	−91.6878649	−24.5385682	−24.5385691	0.0000009
YAMA-23	8	67.1492967	−91.6878649	−24.5385682	−24.5385691	0.0000009
YAMA-IV	0	33.8706511	−42.3795985	−8.5089475	−8.5089478	0.0000003
YAMA-IV	2	33.8831066	−42.4040312	−8.5209246	−8.5209249	0.0000003
YAMA-IV	4	33.8830798	−42.4040352	−8.5209554	−8.5209557	0.0000003
YAMA-IV	6	33.8830794	−42.4040350	−8.5209555	−8.5209558	0.0000003
YAMA-IV	8	33.8830794	−42.4040350	−8.5209555	−8.5209558	0.0000003

TABLE IV. Expectation values $\langle H\rangle$, $\langle H_0\rangle$, $\langle V\rangle$, and three-body binding energy E_3 for the Yamaguchi potentials within the 2D approach, shown as a function of the maximum two-body angular momentum $l_{\max}$, with $q_{\rm cut} = 400$ fm^{-1} ($p_{\rm cut} = 600$ fm^{-1}) and $N_p = N_q = 768$ points.

Potential	$l_{\max}$	$\langle H_0\rangle$ [MeV]	$\langle V\rangle$ [MeV]	$\langle H\rangle$ [MeV]	E_3 [MeV]	$\lvert E_3 - \langle H\rangle\rvert$ [MeV]
YAMA-23	0	67.1444152	−91.6722913	−24.5278761	−24.5278776	0.0000015
YAMA-23	2	67.1492911	−91.6878496	−24.5385585	−24.5385600	0.0000015
YAMA-23	4	67.1492787	−91.6878468	−24.5385681	−24.5385697	0.0000015
YAMA-23	6	67.1492787	−91.6878468	−24.5385681	−24.5385697	0.0000015
YAMA-23	8	67.1492787	−91.6878468	−24.5385681	−24.5385697	0.0000015
YAMA-IV	0	33.8706473	−42.3795948	−8.5089474	−8.5089480	0.0000006
YAMA-IV	2	33.8831029	−42.4040275	−8.5209246	−8.5209252	0.0000006
YAMA-IV	4	33.8830761	−42.4040315	−8.5209554	−8.5209559	0.0000006
YAMA-IV	6	33.8830757	−42.4040312	−8.5209555	−8.5209561	0.0000006
YAMA-IV	8	33.8830757	−42.4040312	−8.5209555	−8.5209561	0.0000006

TABLE V. Expectation values $\langle H\rangle$, $\langle H_0\rangle$, $\langle V\rangle$, and three-body binding energy E_3 calculated for the Yamaguchi potentials within the three-dimensional scheme (3D), using $q_{\rm cut} = 400$ fm^{-1} ($p_{\rm cut} = 600$ fm^{-1}), $N_p = N_q = 512$ and $N_x = 34$ mesh points.

Potential	$l_{\max}$	$\langle H_0\rangle$ [MeV]	$\langle V\rangle$ [MeV]	$\langle H\rangle$ [MeV]	E_3 [MeV]	$\lvert E_3 - \langle H\rangle\rvert$ [MeV]
YAMA-23	0	67.1443111	−91.6721857	−24.5278746	−24.5278788	0.0000042
YAMA-23	2	67.1491870	−91.6877440	−24.5385570	−24.5385612	0.0000042
YAMA-23	4	67.1491714	−91.6877380	−24.5385666	−24.5385697	0.0000031
YAMA-23	6	67.1491712	−91.6877378	−24.5385667	−24.5385697	0.0000030
YAMA-23	8	67.1491712	−91.6877378	−24.5385667	−24.5385697	0.0000030
YAMA-IV	0	33.8706252	−42.3795718	−8.5089467	−8.5089492	0.0000025
YAMA-IV	2	33.8830807	−42.4040046	−8.5209238	−8.5209264	0.0000025
YAMA-IV	4	33.8830459	−42.4040005	−8.5209546	−8.5209552	0.0000006
YAMA-IV	6	33.8830448	−42.4039995	−8.5209547	−8.5209552	0.0000004
YAMA-IV	8	33.8830447	−42.4039995	−8.5209547	−8.5209552	0.0000004

partial-wave contributions P_l. As discussed in Sec. III, while the Faddeev components are strictly bounded by the interaction truncation $l_{\max}$, the full wave function Ψ contains an infinite sequence of partial waves generated by the permutation operator. To quantify this extended angular content, we project the full wave function Ψ onto partial waves up to $l = 12$. Table VI presents a detailed comparison of these contributions for the YAMA-23 potential across all three numerical schemes, with the underlying interaction itself truncated at $l_{\max} = 12$.

The results reveal excellent consistency. The dominant $l = 0$ component, which accounts for about 99.154% of the total norm, agrees across the three formulations to better than 4×10^{-7} percentage points. Comparable absolute consistency persists for the higher partial waves, despite their rapidly decreasing

TABLE VI. Comparison of partial-wave contributions P_l (in %) to the total wave function norm for the YAMA-23 potential and $q_{\rm cut} = 400$ fm^{-1} ($p_{\rm cut} = 600$ fm^{-1}). The values are shown to highlight the agreement among the 1D, 2D, and 3D numerical schemes. The wave functions are normalized according to $3\langle\psi|\Psi\rangle = 1$.

$l_{\rm max}$	1D [%]	2D [%]	3D [%]
0	99.15395104	99.15395100	99.15395139
2	0.78070564	0.78070530	0.78070495
4	0.05445832	0.05445770	0.05445755
6	0.00808918	0.00808838	0.00808827
8	0.00185261	0.00185168	0.00185160
10	0.00056014	0.00055912	0.00055906
12	0.00020520	0.00020411	0.00020407
$\langle\Psi\|\Psi\rangle$ [%]	99.99982214	99.99981729	99.99981689

magnitude. This shows that the 3D vector-variable approach accurately reproduces the angular content of the state when projected onto partial waves, even though no partial-wave basis is used in solving the 3D equation.

The final row of Table VI shows that the partial-wave sum through $l = 12$ captures about 99.9998% of the total norm. The remaining deviation from 100% reflects the neglected $l > 12$ tail of the full wave function generated by the permutation operator, while the small differences among the 1D, 2D, and 3D columns reflect the different interpolation and projection procedures used in the three formulations. Thus the comparison demonstrates both the saturation of the partial-wave expansion and the consistency of the 3D vector-variable projection onto partial waves.

The smoothness of the multidimensional calculations is further illustrated by examining the two-dimensional structures of the physical states. Figures 6 and 7 display contour plots of the full three-body wave functions $\Psi_l(p, q)$ alongside their corresponding Faddeev components $\psi_l(p, q)$ for the YAMA-23 potential, spanning partial waves from $l = 0$ up to $l = 10$. For the separable Yamaguchi interaction, the Faddeev components reflect the rank-one structure of the driving interaction, while the full wave functions exhibit the coupled structures generated by the permutation operator. Even in the highly suppressed $l = 10$ channel, the contour lines remain smooth and free of visible numerical artifacts, providing a visual check that the spline interpolations and Gauss–Legendre quadratures handle the shifted momentum arguments smoothly.

B. Two-Dimensional Formulation: t-Matrix vs. Bare Potential

The two-dimensional partial-wave formulation provides a direct test of the potential-driven equation derived in Eq. (32). Unlike the standard formulation, Eq. (30), which uses the fully off-shell two-body t-matrix, the V-driven equation acts directly with the bare interaction and contains both the direct $G_0V|\psi\rangle$ term and the permutation contribution $G_0VP|\psi\rangle$. Agreement between the two formulations therefore tests not only the two-body input, but also the implementation of the permutation geometry.

We perform this comparison for the YAMA-23 interaction in the same truncated partial-wave space used in the benchmark calculations. The interaction includes all even partial waves up to $l_{\rm max} = 12$, and the momentum cutoffs are fixed at $q_{\rm cut} = 400$ fm^{-1} and $p_{\rm cut} = 600$ fm^{-1}.

Table VII summarizes the final converged eigenvalue energies and internal residuals for both approaches, showing that the two formulations converge to the same eigenvalue within the numerical accuracy of the discretization. At the largest evaluated common mesh size ($N_p = N_q = 384$), the t-driven calculation gives $E_3 = -24.5385690$ MeV, while the V-driven calculation gives $E_3 = -24.5385680$ MeV. The absolute difference, 1.0×10^{-6} MeV, is smaller than the corresponding internal residuals. Detailed mesh convergence data establishing these values are provided in Appendix A (Table XVI). This shows that the V-driven equation reproduces the same permutation geometry as the standard t-driven formulation within the quoted numerical accuracy, while avoiding the explicit construction of the fully off-shell two-body t-matrix.

C. Three-Dimensional Vector Formulation: t-Matrix vs. Bare Potential

The three-dimensional (3D) vector-variable formulation provides the most direct test of the multidimensional permutation geometry. In this approach, the wave function is represented as a function of the Jacobi momentum vectors, without expanding it in partial waves. The shifted permutation arguments must therefore be handled directly in the continuous angular variables, requiring multidimensional quadratures and interpolations of the shifted wave-function arguments and, in the t-driven case, of the off-shell two-body t-matrix.

As in the 2D case, we compare the standard t-matrix-driven equation, Eq. (38), with the potential-driven equation, Eq. (40). For a strict comparison with the 1D and 2D benchmarks, the same truncated YAMA-23 interaction space is embedded into the 3D kernel, including even partial waves up to $l_{\rm max} = 12$. The momentum cutoffs are fixed at $q_{\rm cut} = 400$ fm^{-1} and $p_{\rm cut} = 600$ fm^{-1}.

Table VII also presents the direct comparison of the two 3D kernels. Consistent with the 2D results, the t-driven calculation gives $E_3 = -24.5385697$ MeV and the V-driven calculation

TABLE VII. Summary comparison of the three-body binding energies E_3 and internal residuals $\Delta E = |E_3 - \langle H \rangle|$ obtained via the standard t-matrix-driven and the potential-driven (V-driven) formulations. Values reflect the most converged mesh size common to the compared calculations, $N_p = N_q = 384$. The absolute difference $\Delta E_3^{t-V} = |E_3^t - E_3^V|$ quantifies the agreement of the two kernel implementations within the numerical discretization accuracy.

Potential	Formulation	E_3 [MeV]	ΔE [MeV]	ΔE_3^{t-V} [MeV]
YAMA-23 (2D, $l_{\max} = 12$)	t-driven	-24.5385690	0.0000054	0.0000010
	V-driven	-24.5385680	0.0000044	
YAMA-23 (3D, $l_{\max} = 12$)	t-driven	-24.5385697	0.0000030	0.0000015
	V-driven	-24.5385682	0.0000014	
MT-V (2D, $l_{\max} = 12$)	t-driven	-7.7365935	0.0000111	0.0000035
	V-driven	-7.7365900	0.0000075	
MT-V (3D, $l_{\max} = 12$)	t-driven	-7.7365957	0.0000087	0.0000057
	V-driven	-7.7365900	0.0000029	
MT-V (3D, $l_{\max} = \infty$)	t-driven	-7.7366067	0.0000082	0.0000056
	V-driven	-7.7366011	0.0000026	

TABLE VIII. The expectation values $\langle H \rangle$, $\langle H_0 \rangle$, $\langle V \rangle$, and three-body binding energy E_3 calculated for the Malfliet–Tjon potentials within the two-dimensional scheme (2D). The calculations were performed using $N = 512$ mesh points and a momentum cutoff of $q_{\text{cut}} = 200$ fm^{-1}. The final column shows reference binding energies E_3 from Ref. [4] for comparison.

Potential	$l_{\max}$	$\langle H_0 \rangle$ [MeV]	$\langle V \rangle$ [MeV]	$\langle H \rangle$ [MeV]	E_3 [MeV]	$\lvert E_3 - \langle H \rangle \rvert$ [MeV]	E_3 [4] [MeV]
MT-IV	0	76.820039	−101.681869	−24.861830	−24.861869	0.000038	−24.8616
MT-IV	2	77.245094	−102.291805	−25.046711	−25.046751	0.000040	−25.0465
MT-IV	4	77.265189	−102.320617	−25.055428	−25.055468	0.000040	−25.0552
MT-IV	6	77.267671	−102.324183	−25.056512	−25.056553	0.000041	−25.0562
MT-IV	8	77.268189	−102.324928	−25.056739	−25.056781	0.000042	−25.0564
MT-IV	10	77.268338	−102.325142	−25.056804	−25.056846	0.000042	−25.0565
MT-IV	12	77.268391	−102.325218	−25.056827	−25.056870	0.000043	−25.0565
MT-V	0	29.0115917	−36.5513512	−7.5397595	−7.5397624	0.0000029	−7.53975
MT-V	2	29.7092580	−37.4239640	−7.7147060	−7.7147085	0.0000026	−7.71470
MT-V	4	29.7715490	−37.5053881	−7.7338391	−7.7338466	0.0000075	−7.73383
MT-V	6	29.7769602	−37.5130889	−7.7361287	−7.7361372	0.0000085	−7.73613
MT-V	8	29.7775279	−37.5140173	−7.7364894	−7.7364986	0.0000092	−7.73649
MT-V	10	29.7775974	−37.5141613	−7.7365639	−7.7365736	0.0000097	−7.73656
MT-V	12	29.7776046	−37.5141880	−7.7365834	−7.7365935	0.0000100	−7.73658

gives $E_3 = -24.5385682$ MeV at the largest common mesh size. The difference, 1.5×10^{-6} MeV, is again smaller than the corresponding internal residuals. The step-by-step mesh convergence for this 3D comparison is available in Appendix A (Table XVII).

This agreement shows that the V-driven 3D equation reproduces the same permutation geometry as the standard t-driven formulation within the quoted numerical accuracy. It also indicates that the vector-variable interpolation, angular quadrature, and shifted-momentum mappings introduce no detectable systematic discrepancy at this level.

D. Local Interactions: 2D Partial-Wave Convergence

Having established the numerical baseline with soft separable interactions, we next consider local Malfliet–Tjon (MT) potentials in the 2D partial-wave formulation. Compared with the Yamaguchi interactions, these local potentials generate stronger short-range and high-momentum structures in the wave function. Their numerical treatment therefore requires careful control of the momentum cutoff, dense Gauss–Legendre grids, and higher partial-wave truncations in order to obtain stable expectation values.

Tables XVIII and XIX in Appendix A show the cutoff and mesh convergence for the MT-V potential at $l_{\max} = 12$. The internal residual $\Delta E = |E_3 - \langle H \rangle|$ is reduced to approximately 10^{-5} MeV for $q_{\text{cut}} = 200$ fm^{-1} and $N = 512$. Increasing the cutoff to $q_{\text{cut}} = 300$ fm^{-1} lowers the residual only slightly, to 9.4×10^{-6} MeV, indicating that the remaining discrepancy is dominated mainly by the difficulty of the expectation-value integration rather than by the eigenvalue determination.

Table VIII presents the 2D binding energies and expectation values for the MT-IV and MT-V potentials as functions of the

TABLE IX. Expectation values $\langle H\rangle$, $\langle H_0\rangle$, $\langle V\rangle$, and three-body binding energy E_3 calculated for the Malfliet–Tjon potentials within the three-dimensional scheme (3D). The rows labeled $l_{\max} = \infty$ denote calculations with the full vector-variable interaction. Previous full-3D results from Ref. [4] are included for direct comparison.

Potential	$l_{\max}$	$\langle H_0\rangle$ [MeV]	$\langle V\rangle$ [MeV]	$\langle H\rangle$ [MeV]	E_3 [MeV]	$\lvert E_3 - \langle H\rangle\rvert$ [MeV]
MT-IV	0	76.820184	−101.682010	−24.861826	−24.861907	0.000080
MT-IV	2	77.245198	−102.291906	−25.046708	−25.046784	0.000077
MT-IV	4	77.265184	−102.320609	−25.055425	−25.055480	0.000055
MT-IV	6	77.267537	−102.324046	−25.056509	−25.056542	0.000033
MT-IV	8	77.267926	−102.324663	−25.056737	−25.056749	0.000013
MT-IV	10	77.267945	−102.324747	−25.056802	−25.056796	0.000006
MT-IV	12	77.267995	−102.324820	−25.056825	−25.056817	0.000009
MT-IV	∞	77.267335	−102.324189	−25.056854	−25.056768	0.000087
MT-IV [4]	∞	77.2055	−102.2550	−25.0495	−25.0499	0.0003
MT-V	0	29.0115589	−36.5513174	−7.5397585	−7.5397651	0.0000067
MT-V	2	29.7092519	−37.4239578	−7.7147058	−7.7147155	0.0000097
MT-V	4	29.7715359	−37.5053761	−7.7338402	−7.7338498	0.0000096
MT-V	6	29.7769459	−37.5130768	−7.7361308	−7.7361403	0.0000095
MT-V	8	29.7775116	−37.5140038	−7.7364922	−7.7365013	0.0000091
MT-V	10	29.7775791	−37.5141463	−7.7365672	−7.7365761	0.0000089
MT-V	12	29.7775867	−37.5141737	−7.7365870	−7.7365957	0.0000087
MT-V	∞	29.7775830	−37.5141815	−7.7365985	−7.7366067	0.0000082
MT-V [4]	∞	29.77706	−37.51340	−7.73634	−7.73650	0.00011

TABLE X. Comparison of partial-wave norm contributions and global expectation values evaluated in momentum space and coordinate space for the YAMA-23 and MT-V potentials in the 2D approach. $l_{\max} = 12$ and $q_{\rm cut} = 400$ fm^{-1} ($p_{\rm cut} = 600$ fm^{-1}) for YAMA-23 and $q_{\rm cut} = 200$ fm^{-1} ($p_{\rm cut} = 300$ fm^{-1}) for MT-V. The wave functions are normalized according to $3\langle\psi|\Psi\rangle = 1$. Previous values for the MT-V norm contributions and expectation values from Ref. [4] are included for comparison.

	YAMA-23		MT-V		
$l_{\max}$	Momentum space	Coordinate space	Momentum space	Coordinate space	Ref. [4]
0	99.15395100	99.15395431	99.08519532	99.08518248	99.0851
2	0.78070530	0.78070529	0.74823192	0.74822946	0.7482
4	0.05445770	0.05445766	0.11591648	0.11591595	0.1159
6	0.00808838	0.00808835	0.03304501	0.03304576	0.03305
8	0.00185168	0.00185167	0.01087725	0.01087857	0.01088
10	0.00055912	0.00055911	0.00393585	0.00393723	0.003939
12	0.00020411	0.00020410	0.00154116	0.00154233	0.001545
$\langle\Psi\|\Psi\rangle$ [%]	99.99981729	99.99982049	99.99874300	99.99873178	99.998614
$\langle H_0\rangle$ [MeV]	67.1492787	67.1495505	29.7776046	29.7776111	29.77760
$\langle V\rangle$ [MeV]	−91.6878468	−91.6878500	−37.5141880	−37.5141737	−37.51390
$\langle H\rangle$ [MeV]	−24.5385681	−24.5382995	−7.7365834	−7.7365627	−7.73634

maximum two-body angular momentum $l_{\max}$. In contrast to the separable Yamaguchi interactions, the local MT potentials exhibit a slower partial-wave convergence. Higher partial waves remain numerically relevant, and the binding energies stabilize only around $l_{\max} = 10$–12 at the displayed precision. This behavior reflects the stronger short-range structure of the local interactions, which generates more pronounced high-momentum and higher-partial-wave components than the soft separable Yamaguchi potentials.

For comparison, Table VIII additionally includes previous binding energy calculations from Ref. [4]. The agreement is consistent with their reported four- to five-digit precision, while the extended integration meshes used here ($N_p = N_q = 512$) stabilize additional digits and reduce the internal expectation-value residuals.

Despite these more demanding convergence properties, the 2D formulation remains stable. At $l_{\max} = 12$, the final MT-V result is $E_3 = -7.7365935$ MeV with $\Delta E = 1.0 \times 10^{-5}$ MeV, while MT-IV gives $E_3 = -25.056870$ MeV with $\Delta E = 4.3 \times 10^{-5}$ MeV. These values provide the local interaction benchmark against which the 3D vector-variable calculations are compared below.

Table VII compares the corresponding converged t-driven and V-driven 2D kernels for the MT-V potential. The two

TABLE XI. Comparison of partial-wave norm contributions and global expectation values evaluated in momentum space and coordinate space for the YAMA-23 and MT-V potentials in the 3D approach. The wave functions are normalized according to $3\langle\psi|\Psi\rangle = 1$.

	YAMA-23		MT-V	
$l_{\max}$	Momentum space	Coordinate space	Momentum space	Coordinate space
0	99.15395139	99.15396651	99.08519145	99.08523217
2	0.78070495	0.78070513	0.74823417	0.74823133
4	0.05445755	0.05445752	0.11591663	0.11591863
6	0.00808827	0.00808825	0.03304505	0.03304942
8	0.00185160	0.00185158	0.01087728	0.01088270
10	0.00055906	0.00055905	0.00393587	0.00394164
12	0.00020407	0.00020406	0.00154117	0.00154690
$\langle\Psi\|\Psi\rangle$ [%]	99.99981689	99.99983210	99.99874162	99.99880277
$\langle H_0\rangle$ [MeV]	67.1491213	67.1494527	29.7776240	29.7768789
$\langle V\rangle$ [MeV]	−91.6876644	−91.6877642	−37.5142040	−37.5141943
$\langle H\rangle$ [MeV]	−24.5385431	−24.5383116	−7.7365790	−7.7373154

eigenvalue energies differ by only 3.5×10^{-6} MeV (with detailed step-by-step convergence shown in Appendix A, Table XX). Thus the agreement observed for the separable YAMA-23 benchmark also persists for a local interaction with stronger short-range structure.

E. Three-Dimensional Vector Formulation for Local Interactions

The local interactions are also tested in the full 3D vector-variable formulation. Table XXIII in Appendix A shows the cutoff convergence for the MT-V potential using the truncated interaction space with $l_{\max} = 12$. The convergence pattern is consistent with the 2D calculation: increasing the cutoff from 60 fm^{-1} to 200 fm^{-1} reduces the internal residual from 4.6×10^{-5} MeV to 8.9×10^{-6} MeV, while a further increase to 300 fm^{-1} changes the residual only slightly.

Table IX presents the corresponding 3D vector-variable results for the MT-IV and MT-V potentials. For the truncated interaction spaces, the convergence pattern closely follows the 2D partial-wave calculation. The binding energies stabilize by $l_{\max} = 10$–12 at the displayed precision, showing that the 3D vector-variable kernel reproduces the partial-wave convergence pattern when the same finite interaction space is embedded into the 3D formulation.

For MT-V at $l_{\max} = 12$, the 3D calculation gives $E_3 = -7.7365957$ MeV with $\Delta E = 8.7 \times 10^{-6}$ MeV, in close agreement with the corresponding 2D result $E_3 = -7.7365935$ MeV. For MT-IV, the corresponding 3D result is $E_3 = -25.056817$ MeV, compared with $E_3 = -25.056870$ MeV in the 2D calculation. The remaining differences are at the level expected from the different quadratures, interpolation procedures, and grid sizes.

The rows labeled $l_{\max} = \infty$ use the full vector-variable Malfliet–Tjon interaction rather than an embedded finite partial-wave truncation. These calculations therefore provide the direct 3D local-potential benchmark. For MT-V, the agreement with the previous full-3D calculation of Ref. [4] is at the 10^{-4} MeV level. The MT-IV full-3D entry shows a larger sensitivity to the precise numerical and interaction conventions, although the finite-$l_{\max}$ convergence pattern remains consistent with the 2D calculation.

Finally, Table VII demonstrates that the excellent agreement between the t-driven and V-driven kernels holds for the MT-V potential in the full 3D continuous space. The available V-driven calculations agree with the corresponding t-driven results within the displayed numerical accuracy (see Tables XXI and XXII in Appendix A for full convergence details). This shows that the potential-driven equation preserves the same permutation geometry as the standard t-driven formulation also in the full vector-variable setting, within the displayed numerical accuracy.

F. Wave Function Analysis and Coordinate-Space Transformation

To investigate the spatial structure of the bound state, we use the Fourier-transform framework developed in Sec. VI to map the converged momentum-space wave functions into coordinate space. This provides an independent check of the wave-function normalization, the partial-wave content, and the expectation values evaluated in the two representations.

Table X compares the partial-wave norm contributions obtained in momentum space with those extracted after the coordinate-space transformation for the YAMA-23 and MT-V potentials in the 2D formulation. The agreement of the individual partial-wave contributions shows that the Fourier–Bessel transformation preserves the angular decomposition of the wave function at high numerical accuracy. For the MT-V potential, we also include previous partial-wave norm calculations from Ref. [4]. The agreement is consistent with the precision of the earlier results, while the denser grids used here provide additional stabilization of the norm and expectation-value diagnostics. The summed norms remain close to the momentum-space normalization, with the small deviations reflecting the combined effects of finite momentum cutoffs, finite coordinate-space grids, and oscillatory quadrature.

The corresponding comparison for the 3D formulation is

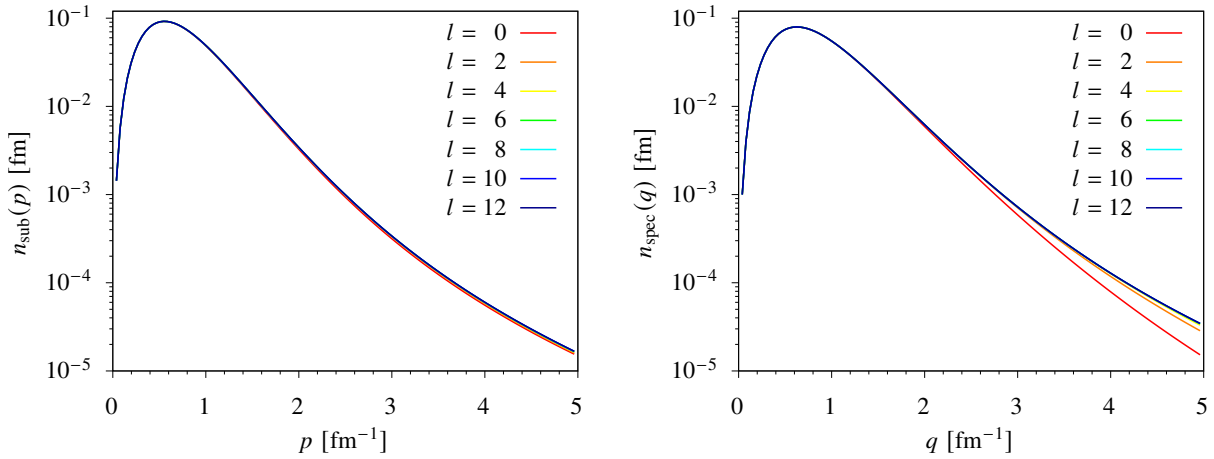


FIG. 2. The momentum distributions $n_{\rm sub}(p)$ and $n_{\rm spec}(q)$ with the YAMA-23 potential in a two-dimensional approach (2D). The curves represent the monotonically increasing partial-wave sums for $l = 0, 2, 4, 6, 8, 10$, and 12.

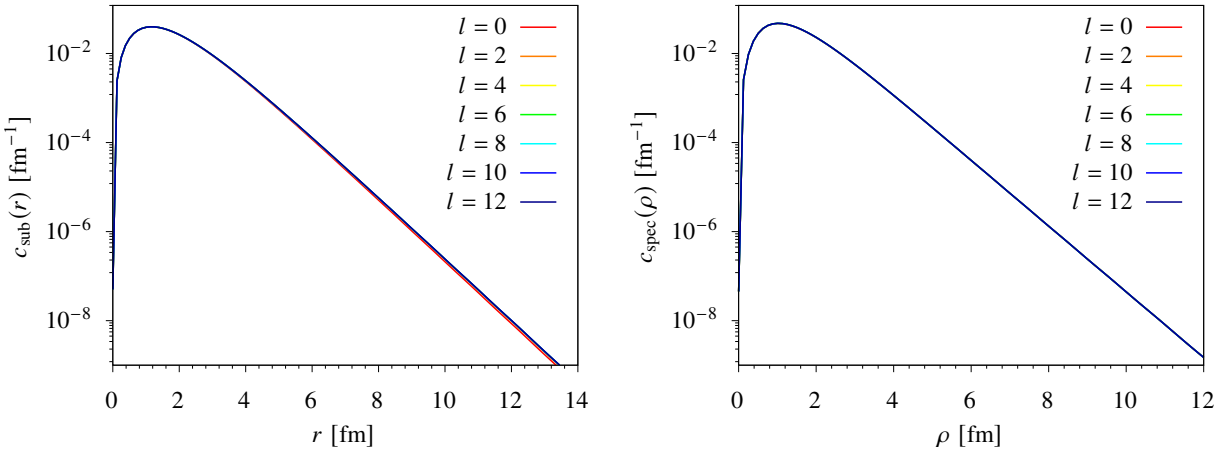


FIG. 3. The spatial pair correlation function $c_{\rm sub}(r)$ and spectator distribution $c_{\rm spec}(\rho)$ with the YAMA-23 potential in a two-dimensional approach (2D). The curves represent the monotonically increasing partial-wave sums for $l = 0, 2, 4, 6, 8, 10$, and 12.

shown in Table XI. As in the 2D case, the partial-wave norm contributions are stable under the coordinate-space transformation. These quantities are much more stable than the Hamiltonian expectation values in the direct 3D coordinate-space transform. The latter involve additional derivative and potential-energy integrations and therefore show larger deviations than the corresponding momentum-space evaluations, providing a measure of the remaining numerical uncertainty associated with the oscillatory coordinate-space integrals.

Figures 2 and 4 show the momentum distributions $n_{\rm sub}(p)$ and $n_{\rm spec}(q)$ for the YAMA-23 and MT-V potentials. Compared with the soft separable Yamaguchi interaction, the local MT-V potential generates a more structured intermediate-momentum region. In particular, the two-body momentum distribution exhibits a pronounced suppression around $p \approx 2$ fm^{-1}, consistent with the interplay between the attractive long-range and repulsive short-range parts of the interaction. (Contour plots of the corresponding 2D partial-wave components and the full 3D vector-variable wave functions are provided for visual reference in Appendices C and D.)

The corresponding coordinate-space information is shown in Figs. 3 and 5. These figures display the pair correlation function $c_{\rm sub}(r)$ and the spectator distribution $c_{\rm spec}(\rho)$ for YAMA-23 and MT-V, respectively. For the MT-V potential, the short-range repulsive component suppresses the pair correlation at small distances. Resolving this depletion requires higher partial waves, in agreement with the slower partial-wave convergence observed for the local interactions in Table VIII.

G. Spatial Geometry and the Equilateral Ideal

The expectation values of the Jacobi coordinates provide a compact measure of the average spatial geometry of the three-body bound state. In the convention used here, $\langle r \rangle$ represents the average pair separation, while $\langle \rho \rangle$ measures the distance of the spectator particle from the center of mass of the interacting pair. Their ratio can therefore be compared with the value $2/\sqrt{3}$ expected for the corresponding Jacobi-coordinate representation of an equilateral triangle.

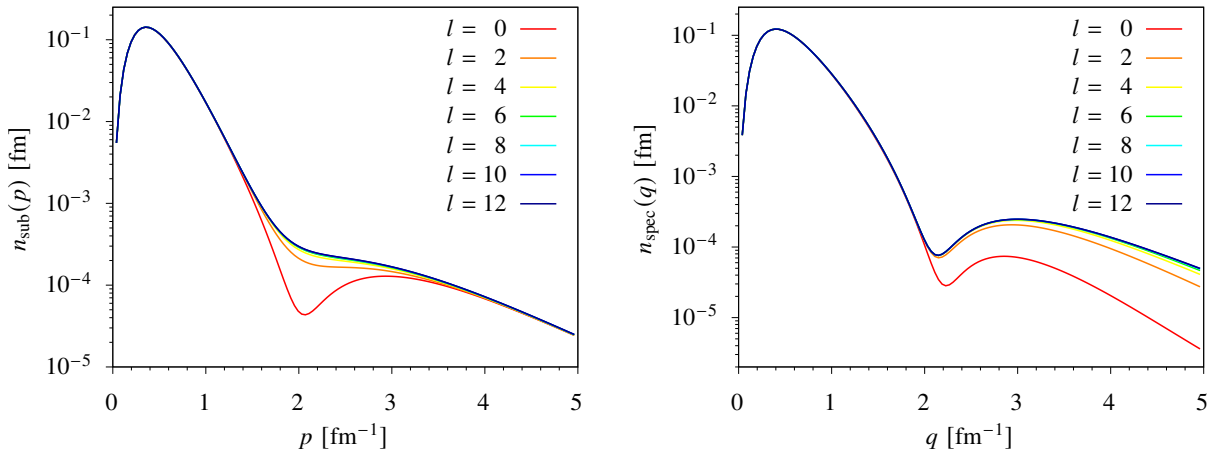


FIG. 4. The momentum distributions $n_{\rm sub}(p)$ and $n_{\rm spec}(q)$ with the MT-V potential in a two-dimensional approach (2D). The curves represent the monotonically increasing partial-wave sums for $l = 0, 2, 4, 6, 8, 10$, and 12.

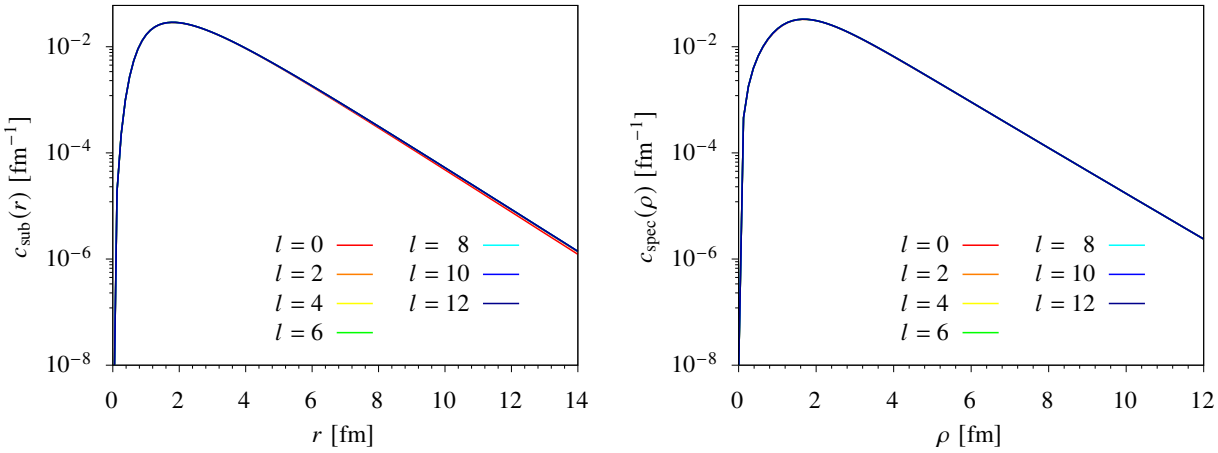


FIG. 5. The spatial pair correlation function $c_{\rm sub}(r)$ and spectator distribution $c_{\rm spec}(\rho)$ with the MT-V potential in a two-dimensional approach (2D). The curves represent the monotonically increasing partial-wave sums for $l = 0, 2, 4, 6, 8, 10$, and 12.

TABLE XII. Comparison of the spatial expectation values and geometric deviation δ for local (MT-V) and separable (YAMA-23) potentials across the 2D and 3D formulations. The 3D results explicitly contrast the embedded finite partial-wave space ($l = 12$) with the full vector-variable interaction ($l = \infty$) to demonstrate spatial convergence. The expected ratio for an ideal equilateral triangle is $2/\sqrt{3} \approx 1.1547$.

Potential	$\langle r\rangle$ [fm]	$\langle \rho\rangle$ [fm]	$\langle r\rangle/\langle\rho\rangle$	δ [%]
2D Approach				
MT-V ($l = 12$)	2.620617	2.270469	1.154219	−0.041728
YAMA-23 ($l = 12$)	1.658895	1.442613	1.149923	−0.413706
3D Approach				
MT-V ($l = \infty$)	2.620616	2.270468	1.154218	−0.041749
MT-V ($l = 12$)	2.620616	2.270468	1.154218	−0.041748
YAMA-23 ($l = 12$)	1.658895	1.442613	1.149923	−0.413727

Table XII shows that both interactions produce an average Jacobi geometry very close to the equilateral reference value, with deviations well below one percent. Furthermore, the table demonstrates the exceptional stability of these spatial observables across both the 2D and 3D coordinate-space transformations: for the local MT-V potential, expanding the interaction from the truncated $l = 12$ space to the full $l = \infty$ continuous vector space alters the macroscopic spatial expectation values only at the sixth decimal place.

The absolute sizes of these spatial expectation values directly reflect the respective binding energies: the weakly bound MT-V state has a much larger spatial extent ($\langle r\rangle \approx 2.62$ fm) compared with the deeply bound YAMA-23 state ($\langle r\rangle \approx 1.66$ fm).

Despite their drastically different spatial extents and short-range structures, the average geometric proportions of both states are highly symmetric. For the local MT-V potential, the macroscopic interplay of long-range attraction and short-range repulsion produces an average geometry that is very close to the equilateral reference value ($\delta \simeq -0.04\%$). For the softer separable YAMA-23 interaction, the ratio is only slightly smaller than the equilateral ideal ($\delta \simeq -0.41\%$). These deviations should not be interpreted as a pointwise geometric constraint on the wave function, but rather as a compact diagnostic of the

average spatial correlations of the bound state.

H. Numerical Error Budget

To consolidate the convergence properties discussed above, we quantify the dominant numerical uncertainties of the calculation. The accuracy of the three-body binding energies and expectation values is controlled mainly by four sources:

1. Discretization and Cutoff Error: As demonstrated in the convergence tables, truncating the semi-infinite momentum domains at $q_{\rm cut} = 400$ fm^{-1} ($p_{\rm cut} = 600$ fm^{-1}) for Yamaguchi and $q_{\rm cut} = 200$ fm^{-1} ($p_{\rm cut} = 300$ fm^{-1}) for Malfliet–Tjon, combined with dense Gauss–Legendre grids ($N_p = N_q \geq 384$), stabilizes the binding energies to $O(10^{-6})$ MeV. The corresponding expectation values $\langle H_0 \rangle$ and $\langle V \rangle$ are more sensitive to the high-momentum tails but remain stable at the few-10^{-5} MeV level for the most demanding local cases.

2. Interpolation and Kernel-Implementation Error: The evaluation of the shifted permutation arguments requires interpolation of the wave function and, in the t-driven formulations, of the fully off-shell two-body t-matrix. The comparison between the standard t-driven formulation and the V-driven formulation provides a stringent combined check of the interpolation, quadrature, and permutation-kernel implementation. For the Yamaguchi benchmark, the two approaches agree at the 10^{-6} MeV level, while for the local MT-V interaction the agreement is at the few-10^{-6} MeV level. These differences are comparable to or smaller than the corresponding internal residuals.

3. Partial-Wave Truncation Error: For the local MT potentials, the partial-wave expansion converges more slowly than for the separable Yamaguchi interactions. By comparing the embedded $l_{\rm max} = 12$ interaction with the full vector-variable interaction in the 3D approach, we estimate the residual truncation error. For MT-V, omitting $l > 12$ changes the binding energy by approximately 1.1×10^{-5} MeV; for MT-IV, the corresponding change is approximately 5.0×10^{-5} MeV.

4. Coordinate-Space Transformation Error: Mapping the 3D wave functions into configuration space introduces oscillatory quadrature errors. The hybrid Filon integration conserves the wave-function norm to within $O(10^{-4})$ percentage points. The Hamiltonian expectation value is more sensitive: in the direct 3D coordinate-space representation, $\langle H \rangle$ differs from the corresponding momentum-space evaluation by about 5×10^{-3} MeV for YAMA-23 and by a smaller amount for MT-V. This reflects the numerical stiffness of the direct oscillatory spatial-gradient and potential-energy integrals.

In summary, the internal consistency of the three-body calculations is established at the 10^{-6} MeV level for the separable benchmarks and at the few-10^{-6} to 10^{-5} MeV level for the local MT calculations. The residual $\Delta E = |E_3 - \langle H \rangle|$ provides a useful diagnostic of the accuracy of the reconstructed wave functions and expectation-value integrations.

X. SUMMARY AND OUTLOOK

We presented a high-precision momentum-space benchmark of the three-boson bound state, comparing 1D spectator-amplitude, 2D partial-wave, and 3D vector-variable formulations. By embedding identical finite partial-wave interaction spaces across the formulations, the comparison is performed in the same truncated model space, so that remaining differences reflect discretization, interpolation, quadrature, and permutation-geometry effects.

For local Malfliet–Tjon potentials, stronger short-range structures require partial waves up to $l_{\rm max} \approx 10$–12 to stabilize binding energies. Despite this numerical stiffness, internal residuals $|E_3 - \langle H \rangle|$ remain controlled at the $O(10^{-5})$ MeV level, supporting the accuracy of the multidimensional quadrature and interpolation schemes.

A central result is the validation of the vector-variable formulation. Comparing the standard t-matrix-driven Faddeev equation with an alternative bare-potential-driven formulation, we showed that these structurally distinct kernels yield binding energies agreeing at the 10^{-6} MeV level for the Yamaguchi benchmark and few-10^{-6} MeV level for the MT interaction. This provides a stringent validation of the permutation geometry and multidimensional integration machinery, showing that the continuous angular dependence can be accurately resolved without an explicit partial-wave expansion.

We also transformed the converged momentum-space wave functions into coordinate space via 2D double spherical Bessel transforms and 3D Filon-stabilized multidimensional Fourier transforms. The resulting norm decompositions provide a sensitive consistency check. While Hamiltonian expectation values are more demanding in the direct 3D spatial transform (with uncertainties around 5×10^{-3} MeV), the extracted spatial expectation values confirm that the mean geometry of the three-boson ground state remains close to an equilateral reference configuration.

These methods provide a robust framework for momentum-space few-body calculations with and without partial-wave decompositions. Future work will extend this formulation to three-body scattering, where the vector-variable approach is expected to be advantageous by avoiding the proliferation of coupled partial waves. Finally, the validated 3D machinery is well suited for realistic physical systems, particularly for studying the structural properties and low-energy dynamics of weakly bound atomic trimers like noble-gas clusters.

ACKNOWLEDGMENTS

We would like to thank M. Hadizadeh for fruitful discussions, as well as for the generous provision of computational resources at the Ohio Supercomputer Center (OSC) that made this work possible.

Appendix A: Mesh and momentum cutoff convergence tables

TABLE XIII. Convergence of the three-body expectation values for the YAMA-23 potential within the 1D approach at $l_{\max} = 12$ as a function of the momentum cutoff q_{cut}. The wave function has been calculated with $N_p = N_q = 768$ mesh points.

q_{cut} [fm^{-1}]	$\langle H_0 \rangle$ [MeV]	$\langle V \rangle$ [MeV]	$\langle H \rangle$ [MeV]	E_3 [MeV]	$\lvert E_3 - \langle H \rangle \rvert$ [MeV]
40	67.1486391	−91.6865494	−24.5379103	−24.5385691	0.0006588
60	67.1491022	−91.6874758	−24.5383737	−24.5385691	0.0001955
80	67.1492150	−91.6877015	−24.5384865	−24.5385691	0.0000826
100	67.1492552	−91.6877819	−24.5385267	−24.5385691	0.0000424
150	67.1492849	−91.6878413	−24.5385564	−24.5385691	0.0000128
200	67.1492921	−91.6878557	−24.5385636	−24.5385691	0.0000055
300	67.1492958	−91.6878631	−24.5385673	−24.5385691	0.0000018
400	67.1492967	−91.6878649	−24.5385682	−24.5385691	0.0000009
600	67.1492972	−91.6878659	−24.5385687	−24.5385691	0.0000005

TABLE XIV. Convergence of the three-body binding energy E_3 obtained directly from the 1D spectator amplitude equation for the YAMA-23 potential at $l_{\max} = 12$.

q_{cut} [fm^{-1}]	E_3 [MeV]	N
10	−24.53848452	48
20	−24.53856898	48
30	−24.53856914	48
40	−24.53856914	48
50	−24.53856914	48
100	−24.53856914	48

TABLE XV. Mesh convergence of the three-body expectation values for the YAMA-23 potential within the 1D approach at $l_{\max} = 12$, evaluated at a fixed momentum cutoff of $q_{\text{cut}} = 400$ fm^{-1}.

N	$\langle H_0 \rangle$ [MeV]	$\langle V \rangle$ [MeV]	$\langle H \rangle$ [MeV]	E_3 [MeV]	$\lvert E_3 - \langle H \rangle \rvert$ [MeV]
64	67.1461233	−91.6795865	−24.5334632	−24.5385691	0.0051059
96	67.1486518	−91.6862016	−24.5375499	−24.5385691	0.0010193
128	67.1490834	−91.6873256	−24.5382422	−24.5385691	0.0003269
192	67.1492489	−91.6877522	−24.5385032	−24.5385691	0.0000659
256	67.1492753	−91.6878231	−24.5385478	−24.5385691	0.0000214
384	67.1492852	−91.6878496	−24.5385643	−24.5385691	0.0000048
512	67.1492870	−91.6878542	−24.5385672	−24.5385691	0.0000020
768	67.1492877	−91.6878559	−24.5385682	−24.5385691	0.0000009

TABLE XVI. Comparison of the t-matrix-driven and potential-driven (V-driven) 2D formulations for the YAMA-23 potential with $l_{\max} = 12$ and $q_{\rm cut} = 400$ fm^{-1}. Expectation values $\langle H_0\rangle$, $\langle V\rangle$, $\langle H\rangle$, the three-body binding energy E_3, and the residual $|E_3 - \langle H\rangle|$ are shown.

	t-driven approach				V-driven approach			
N	$\langle H_0\rangle$ [MeV]	$\langle V\rangle$ [MeV]	E_3 [MeV]	$\lvert E_3 - \langle H\rangle\rvert$ [MeV]	$\langle H_0\rangle$ [MeV]	$\langle V\rangle$ [MeV]	E_3 [MeV]	$\lvert E_3 - \langle H\rangle\rvert$ [MeV]
128	67.1487913	−91.6869525	−24.5385237	0.0003625	67.1488427	−91.6870039	−24.5385284	0.0003672
192	67.1492014	−91.6876902	−24.5385618	0.0000729	67.1492076	−91.6876965	−24.5385608	0.0000719
256	67.1492081	−91.6877513	−24.5385634	0.0000202	67.1492680	−91.6878113	−24.5385660	0.0000228
384	67.1492713	−91.6878349	−24.5385690	0.0000054	67.1492907	−91.6878543	−24.5385680	0.0000044
512	67.1492758	−91.6878427	−24.5385691	0.0000022	67.1492943	−91.6878612	−24.5385683	0.0000014
768	67.1492787	−91.6878468	−24.5385697	0.0000015	67.1492958	−91.6878639	−24.5385684	0.0000003

TABLE XVII. Comparison of the t-matrix-driven and potential-driven (V-driven) 3D formulations for the YAMA-23 potential with $l_{\max} = 12$ and $q_{\rm cut} = 400$ fm^{-1}. Expectation values $\langle H_0\rangle$, $\langle V\rangle$, the three-body binding energy E_3, and the residual $|E_3 - \langle H\rangle|$ are shown.

	t-driven approach				V-driven approach			
N	$\langle H_0\rangle$ [MeV]	$\langle V\rangle$ [MeV]	E_3 [MeV]	$\lvert E_3 - \langle H\rangle\rvert$ [MeV]	$\langle H_0\rangle$ [MeV]	$\langle V\rangle$ [MeV]	E_3 [MeV]	$\lvert E_3 - \langle H\rangle\rvert$ [MeV]
128	67.1480852	−91.6862463	−24.5384474	0.0002863	67.1480739	−91.6862351	−24.5384351	0.0002739
192	67.1490228	−91.6875116	−24.5385495	0.0000608	67.1490418	−91.6875307	−24.5385371	0.0000482
256	67.1491213	−91.6876644	−24.5385671	0.0000240	67.1492396	−91.6877828	−24.5385656	0.0000224
384	67.1491625	−91.6877259	−24.5385689	0.0000056	67.1492840	−91.6878476	−24.5385675	0.0000039
512	67.1491712	−91.6877378	−24.5385697	0.0000030	67.1492929	−91.6878598	−24.5385682	0.0000014

TABLE XVIII. Momentum cutoff convergence of the three-body expectation values for the MT-V potential in the 2D approach at $l_{\max} = 12$, evaluated on a fixed dense grid of $N = 512$ points.

$q_{\rm cut}$ [fm^{-1}]	$\langle H_0\rangle$ [MeV]	$\langle V\rangle$ [MeV]	$\langle H\rangle$ [MeV]	E_3 [MeV]	$\lvert E_3 - \langle H\rangle\rvert$ [MeV]
60	29.7775714	−37.5141177	−7.7365463	−7.7365935	0.0000471
80	29.7775909	−37.5141596	−7.7365687	−7.7365935	0.0000247
100	29.7775987	−37.5141752	−7.7365765	−7.7365935	0.0000170
150	29.7776029	−37.5141850	−7.7365821	−7.7365935	0.0000114
200	29.7776046	−37.5141880	−7.7365834	−7.7365935	0.0000100
300	29.7776098	−37.5141938	−7.7365841	−7.7365935	0.0000094

TABLE XIX. Mesh convergence of the three-body expectation values for the MT-V potential in the 2D approach with $l_{\max} = 12$, evaluated at a fixed momentum cutoff of $q_{\rm cut} = 200$ fm^{-1}.

N	$\langle H_0\rangle$ [MeV]	$\langle V\rangle$ [MeV]	$\langle H\rangle$ [MeV]	E_3 [MeV]	$\lvert E_3 - \langle H\rangle\rvert$ [MeV]
64	29.7763543	−37.5110421	−7.7346878	−7.7366295	0.0019417
96	29.7773495	−37.5135787	−7.7362292	−7.7366025	0.0003733
128	29.7775183	−37.5139908	−7.7364725	−7.7365960	0.0001235
192	29.7775796	−37.5141411	−7.7365615	−7.7365942	0.0000327
384	29.7776037	−37.5141861	−7.7365824	−7.7365935	0.0000111
512	29.7776046	−37.5141880	−7.7365834	−7.7365935	0.0000100

TABLE XX. Comparison of the t-matrix-driven and potential-driven (V-driven) 2D formulations for the MT-V potential with $l_{\max} = 12$ and $q_{\text{cut}} = 200$ fm^{-1}. Expectation values $\langle H_0 \rangle$, $\langle V \rangle$, the three-body binding energy E_3, and the residual $|E_3 - \langle H \rangle|$ are shown.

	t-driven approach				V-driven approach			
N	$\langle H_0 \rangle$ [MeV]	$\langle V \rangle$ [MeV]	E_3 [MeV]	$\lvert E_3 - \langle H \rangle \rvert$ [MeV]	$\langle H_0 \rangle$ [MeV]	$\langle V \rangle$ [MeV]	E_3 [MeV]	$\lvert E_3 - \langle H \rangle \rvert$ [MeV]
128	29.7775183	−37.5139908	−7.7365960	0.0001235	29.7775337	−37.5140062	−7.7366010	0.0001285
192	29.7775796	−37.5141411	−7.7365942	0.0000327	29.7776093	−37.5141528	−7.7365915	0.0000480
256	29.7776002	−37.5141769	−7.7365936	0.0000169	29.7776092	−37.5141776	−7.7365903	0.0000219
384	29.7776037	−37.5141861	−7.7365935	0.0000111	29.7776049	−37.5141873	−7.7365900	0.0000075

TABLE XXI. Comparison of the t-matrix-driven and potential-driven (V-driven) 3D formulations for the MT-V potential with $l_{\max} = 12$ and $q_{\text{cut}} = 200$ fm^{-1}. Expectation values $\langle H_0 \rangle$, $\langle V \rangle$, the three-body binding energy E_3, and the residual $|E_3 - \langle H \rangle|$ are shown.

	t-driven approach				V-driven approach			
N	$\langle H_0 \rangle$ [MeV]	$\langle V \rangle$ [MeV]	E_3 [MeV]	$\lvert E_3 - \langle H \rangle \rvert$ [MeV]	$\langle H_0 \rangle$ [MeV]	$\langle V \rangle$ [MeV]	E_3 [MeV]	$\lvert E_3 - \langle H \rangle \rvert$ [MeV]
128	29.7777583	−37.5142357	−7.7366735	0.0001961	29.7776559	−37.5141334	−7.7366706	0.0001931
192	29.7776117	−37.5141778	−7.7366096	0.0000434	29.7776174	−37.5141836	−7.7366044	0.0000382
256	29.7775720	−37.5141533	−7.7365988	0.0000175	29.7776097	−37.5141911	−7.7365933	0.0000119
384	29.7775867	−37.5141737	−7.7365957	0.0000087	29.7776091	−37.5141962	−7.7365900	0.0000029

TABLE XXII. Comparison of the t-matrix-driven and potential-driven (V-driven) 3D formulations for the MT-V potential using the full vector-variable interaction rather than a truncated partial-wave representation, with $q_{\text{cut}} = 200$ fm^{-1}. Expectation values $\langle H_0 \rangle$, $\langle V \rangle$, the three-body binding energy E_3, and the residual $|E_3 - \langle H \rangle|$ are shown.

	t-driven approach				V-driven approach			
N	$\langle H_0 \rangle$ [MeV]	$\langle V \rangle$ [MeV]	E_3 [MeV]	$\lvert E_3 - \langle H \rangle \rvert$ [MeV]	$\langle H_0 \rangle$ [MeV]	$\langle V \rangle$ [MeV]	E_3 [MeV]	$\lvert E_3 - \langle H \rangle \rvert$ [MeV]
128	29.7777546	−37.5142440	−7.7366844	0.0001950	29.7776553	−37.5141447	−7.7366818	0.0001924
192	29.7776080	−37.5141857	−7.7366206	0.0000429	29.7776165	−37.5141943	−7.7366156	0.0000378
256	29.7775682	−37.5141611	−7.7366098	0.0000170	29.7776089	−37.5142017	−7.7366044	0.0000116
384	29.7775830	−37.5141815	−7.7366067	0.0000082	29.7776082	−37.5142068	−7.7366011	0.0000026

TABLE XXIII. Momentum cutoff convergence of the three-body expectation values for the MT-V potential in the 3D approach at $l_{\max} = 12$, evaluated on a fixed dense grid of $N = 384$ and $N_x = 50$ points.

q_{cut} [fm^{-1}]	$\langle H_0 \rangle$ [MeV]	$\langle V \rangle$ [MeV]	$\langle H \rangle$ [MeV]	E_3 [MeV]	$\lvert E_3 - \langle H \rangle \rvert$ [MeV]
60	29.7775534	−37.5141033	−7.7365499	−7.7365957	0.0000458
80	29.7775735	−37.5141458	−7.7365723	−7.7365957	0.0000234
100	29.7775839	−37.5141640	−7.7365801	−7.7365959	0.0000159
150	29.7775878	−37.5141734	−7.7365857	−7.7365959	0.0000102
200	29.7775885	−37.5141755	−7.7365870	−7.7365959	0.0000089
300	29.7775885	−37.5141762	−7.7365877	−7.7365959	0.0000082

Appendix B: Explicit Representation of the partial wave projected Permutation Operator

This appendix contains the quantities G and $\tilde{G}$ related to the permutation operators for general total angular momentum $\mathcal{L}$. The function $G_{lLl'L'\mathcal{L}}(q,q',x)$ from Eq. (30) is a combination of Legendre polynomials $P_k(x)$

$$G_{lLl'L'\mathcal{L}}(q,q',x) = \sum_k P_k(x) \sum_{\mu_1+\mu_2=l} \sum_{\nu_1+\nu_2=l'} q'^{\mu_1+\nu_2}\, q^{\mu_2+\nu_1}\, g^{k\mu_1\nu_1\mu_2\nu_2}_{lLl'L'\mathcal{L}}. \tag{B1}$$

For general $\mathcal{L}$ the geometrical coefficient is given as

$$\begin{aligned} g^{k\mu_1\nu_1\mu_2\nu_2}_{lLl'L'\mathcal{L}} = &\sum_{gg'} \hat{k}\,\sqrt{\hat{l}\hat{L}\hat{l}'\hat{L}'}\,\sqrt{\frac{\hat{l}!\,\hat{l}'!}{(2\mu_1)!\,(2\mu_2)!\,(2\nu_1)!\,(2\nu_2)!}} \\ &\times (-)^{l'}\left(\tfrac{1}{2}\right)^{\mu_2+\nu_2}\begin{pmatrix}\mu_2 & L & g\\ 0 & 0 & 0\end{pmatrix}\begin{pmatrix}\nu_2 & L' & g'\\ 0 & 0 & 0\end{pmatrix}\begin{pmatrix}k & \nu_1 & g\\ 0 & 0 & 0\end{pmatrix} \\ &\times \begin{pmatrix}k & \mu_1 & g'\\ 0 & 0 & 0\end{pmatrix}\begin{Bmatrix}\mu_1 & \mu_2 & l\\ L & \mathcal{L} & g\end{Bmatrix}\begin{Bmatrix}\nu_1 & \nu_2 & l'\\ L' & \mathcal{L} & g'\end{Bmatrix}\begin{Bmatrix}\mu_1 & g & \mathcal{L}\\ \nu_1 & g' & k\end{Bmatrix}. \end{aligned} \tag{B2}$$

Here l and L are the relative orbital angular momenta related to p and q. We also use the notation $\hat{l} \equiv 2l+1$.

For the bound state we have $\mathcal{L}=0$, which leads to $l=L$. Then g reduces to

$$\begin{aligned} g^{k\mu_1\nu_1\mu_2\nu_2}_{ll'} = &\sqrt{\frac{\hat{l}\hat{l}'}{\hat{\mu}_1\,\hat{\nu}_1}}\,\sqrt{\frac{\hat{l}!\,\hat{l}'!}{(2\mu_1)!\,(2\mu_2)!\,(2\nu_1)!\,(2\nu_2)!}} \\ &\times \left(\tfrac{1}{2}\right)^{\mu_2+\nu_2}\,(-)^{\mu_1+\nu_1}\begin{pmatrix}\mu_2 & l & \mu_1\\ 0 & 0 & 0\end{pmatrix}\begin{pmatrix}\nu_2 & l' & \nu_1\\ 0 & 0 & 0\end{pmatrix}\begin{pmatrix}\mu_1 & \nu_1 & k\\ 0 & 0 & 0\end{pmatrix}^2 \end{aligned} \tag{B3}$$

and $G_{lLl'L'\mathcal{L}}$ reduces to $G_{ll'}$.

The quantity $\tilde{G}_{lLl'L'\mathcal{L}}(p,q,x)$ occurs in Eq. (22). In the case of general $\mathcal{L}$ the function $\tilde{G}$ reads

$$\tilde{G}_{lLl'L'\mathcal{L}}(p,q,x) = \sum_k P_k(x) \sum_{\mu_1+\mu_2=l'} \sum_{\nu_1+\nu_2=L'} p^{\mu_1+\nu_1}\, q^{\mu_2+\nu_2}\, \tilde{g}^{k\mu_1\nu_1\mu_2\nu_2}_{lLl'L'} \tag{B4}$$

with the geometrical factor

$$\begin{aligned} \tilde{g}^{k\mu_1\nu_1\mu_2\nu_2}_{lLl'L'\mathcal{L}} = &\sum_{gg'} \hat{k}\,\sqrt{\hat{l}'\hat{L}'\hat{g}\hat{g}'}\,\sqrt{\frac{\hat{l}'!\,\hat{L}'!}{(2\mu_1)!\,(2\mu_2)!\,(2\nu_1)!\,(2\nu_2)!}} \\ &\times (-)^{g+L+\nu_2}\left(\tfrac{1}{2}\right)^{\mu_1+\nu_2}\left(\tfrac{3}{4}\right)^{\mu_2}\begin{pmatrix}\mu_1 & \nu_1 & g\\ 0 & 0 & 0\end{pmatrix}\begin{pmatrix}\mu_2 & \nu_2 & g'\\ 0 & 0 & 0\end{pmatrix} \\ &\times \begin{pmatrix}g & k & l\\ 0 & 0 & 0\end{pmatrix}\begin{pmatrix}g' & k & L\\ 0 & 0 & 0\end{pmatrix}\begin{Bmatrix}g' & g & \mathcal{L}\\ l & L & k\end{Bmatrix}\begin{Bmatrix}\mu_1 & \mu_2 & l'\\ \nu_1 & \nu_2 & L'\\ g & g' & \mathcal{L}\end{Bmatrix}. \end{aligned} \tag{B5}$$

Again, for $\mathcal{L}=0$ $\tilde{g}$ reduces to

$$\begin{aligned} \tilde{g}^{k\mu_1\nu_1\mu_2\nu_2}_{ll'} = &\sum_g \hat{k}\,(-)^{\mu_2+g+k}\left(\tfrac{1}{2}\right)^{\mu_1+\nu_2}\sqrt{\frac{\hat{l}'}{\hat{l}}}\,\sqrt{\frac{\hat{l}'!\,\hat{L}'!}{(2\mu_1)!\,(2\mu_2)!\,(2\nu_1)!\,(2\nu_2)!}} \\ &\times \left(\tfrac{3}{4}\right)^{\mu_2}\begin{pmatrix}\mu_1 & \nu_1 & g\\ 0 & 0 & 0\end{pmatrix}\begin{pmatrix}\mu_2 & \nu_2 & g\\ 0 & 0 & 0\end{pmatrix}\begin{pmatrix}g & k & l\\ 0 & 0 & 0\end{pmatrix}^2\begin{Bmatrix}\mu_1 & \mu_2 & l'\\ \nu_2 & \nu_1 & g\end{Bmatrix} \end{aligned} \tag{B6}$$

and correspondingly $\tilde{G}_{lLl'L'\mathcal{L}}$ reduces to $\tilde{G}_{ll'}$.

Appendix C: Momentum-space wave functions for the Yamaguchi and Malfliet–Tjon potentials in the 2D-approach

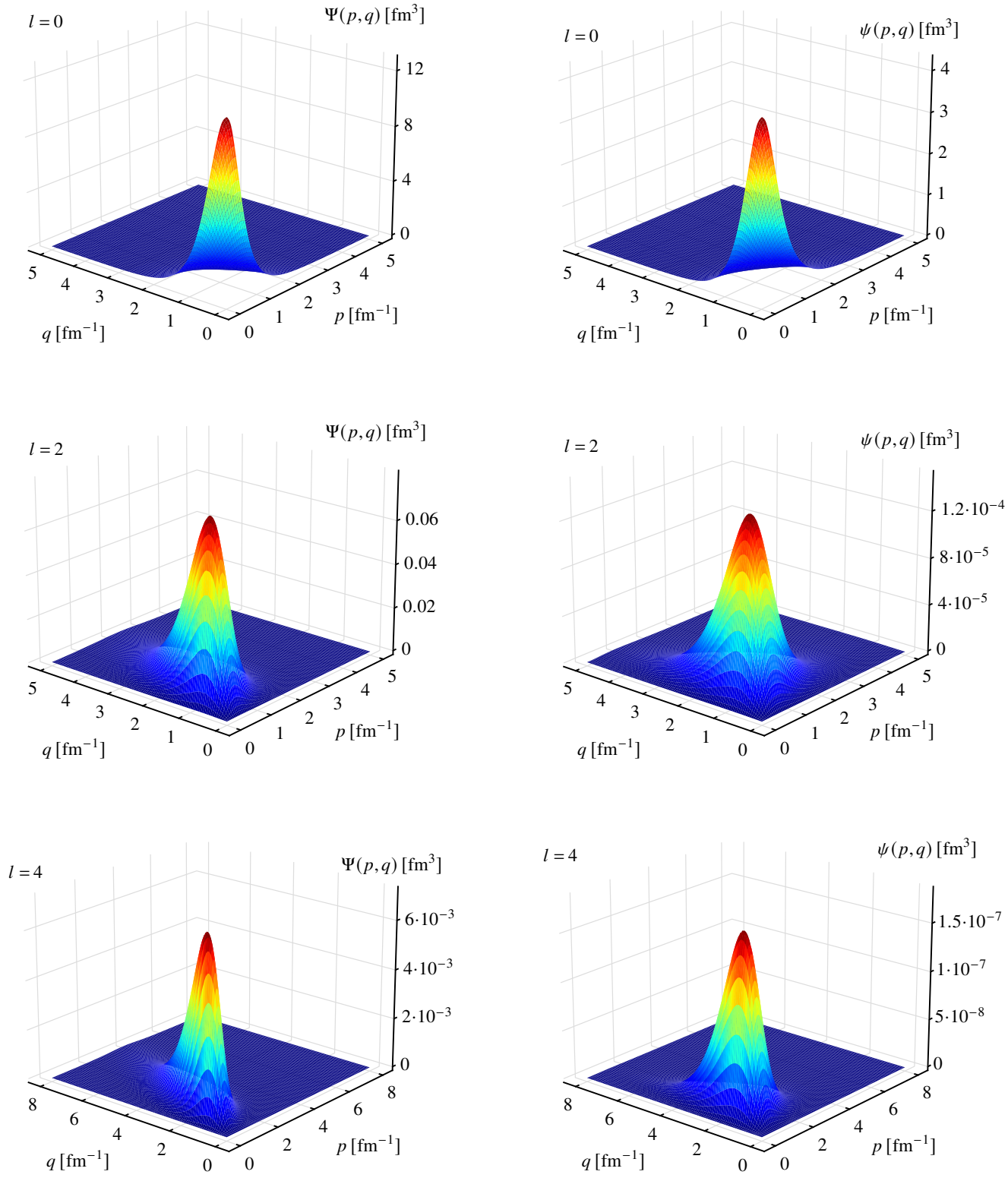


FIG. 6. Three-boson wave functions $\Psi(p,q)$ (left) and the Faddeev components $\psi(p,q)$ (right) with the YAMA-23 potential and the angular momentum $l = 0, 2, 4$ in a 2D approach.

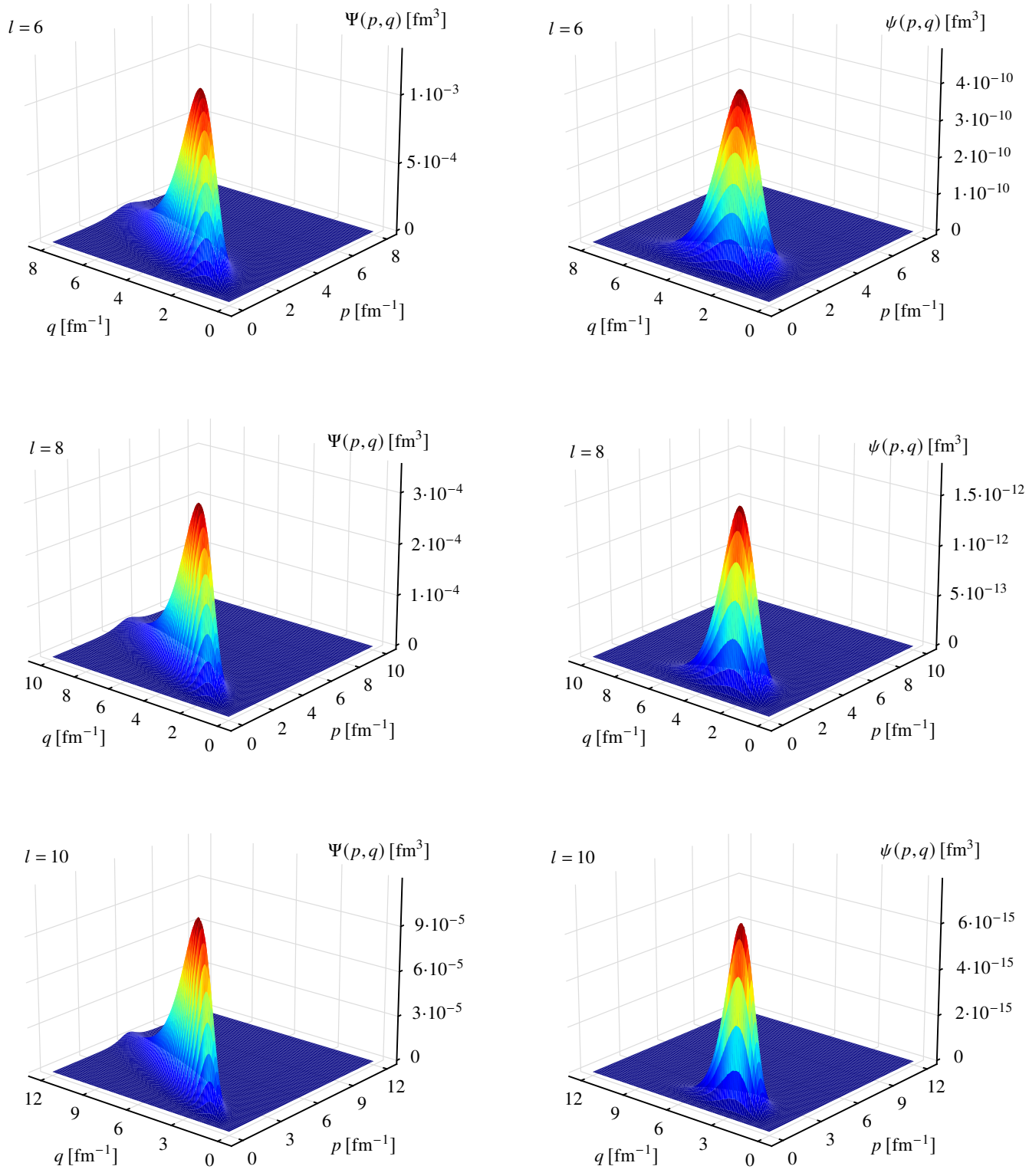


FIG. 7. Three-boson wave functions $\Psi(p,q)$ (left) and the Faddeev components $\psi(p,q)$ (right) with the YAMA-23 potential and the angular momentum $l = 6, 8, 10$ in a two-dimensional approach (2D).

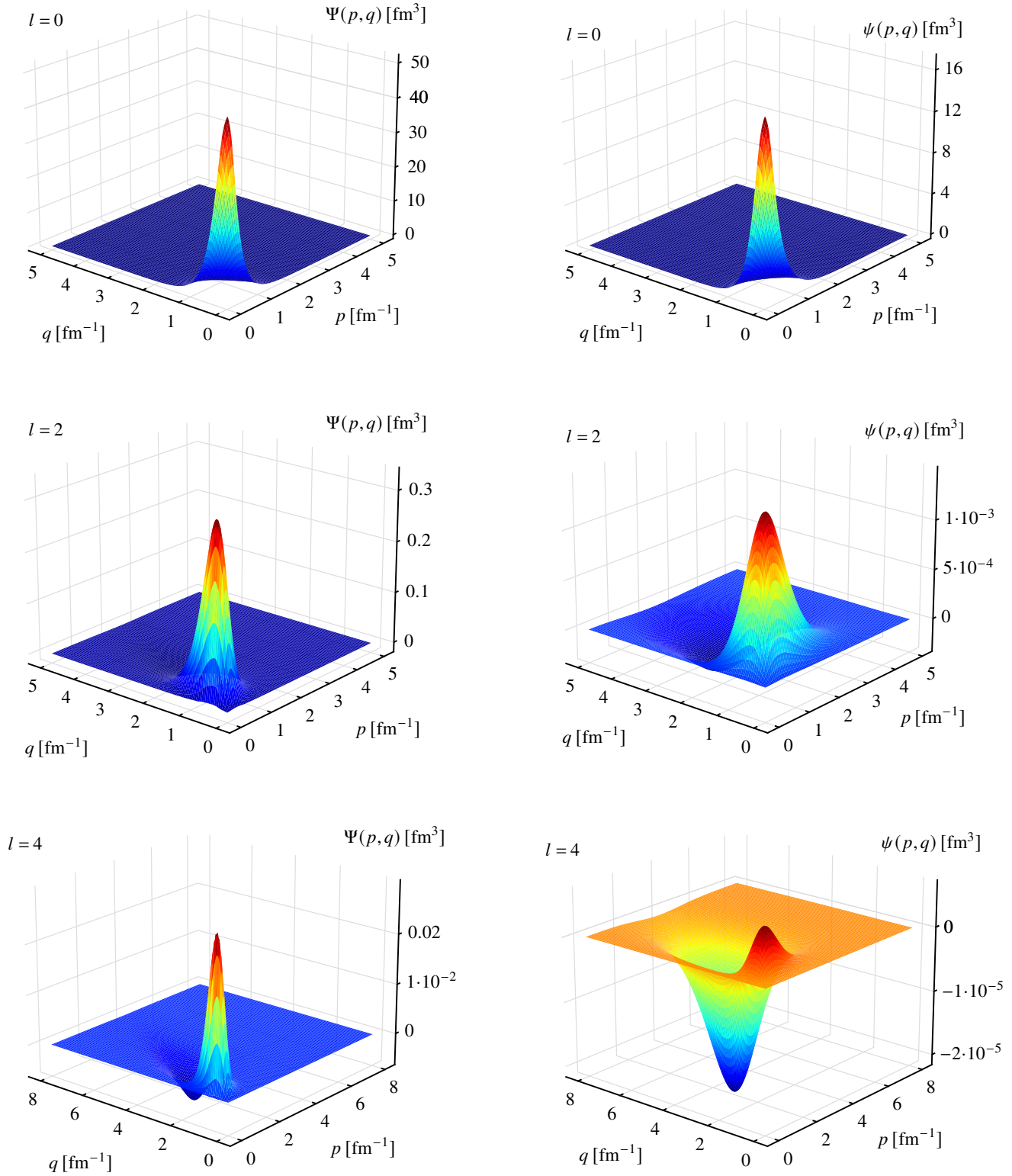


FIG. 8. Three-boson wave functions $\Psi(p,q)$ (left) and the Faddeev components $\psi(p,q)$ (right) with the MT-V potential and the angular momentum $l = 0, 2, 4$ in a two-dimensional approach (2D).

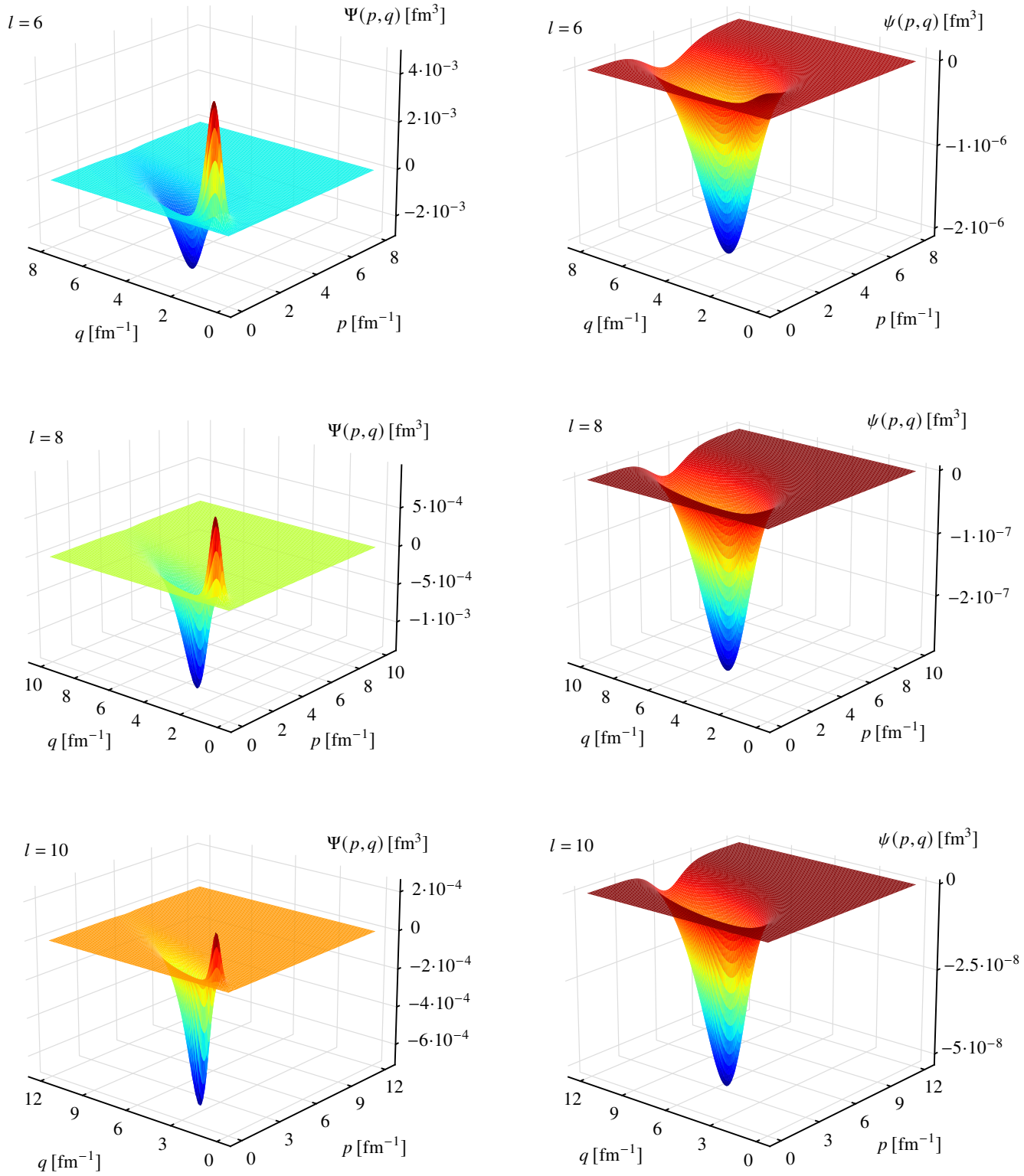


FIG. 9. Three-boson wave functions $\Psi(p,q)$ (left) and the Faddeev components $\psi(p,q)$ (right) with the MT-V potential and the angular momentum $l = 6, 8, 10$ in a two-dimensional approach (2D).

Appendix D: Momentum-space wave functions for the Yamaguchi and Malfliet–Tjon potentials in the 3D-approach

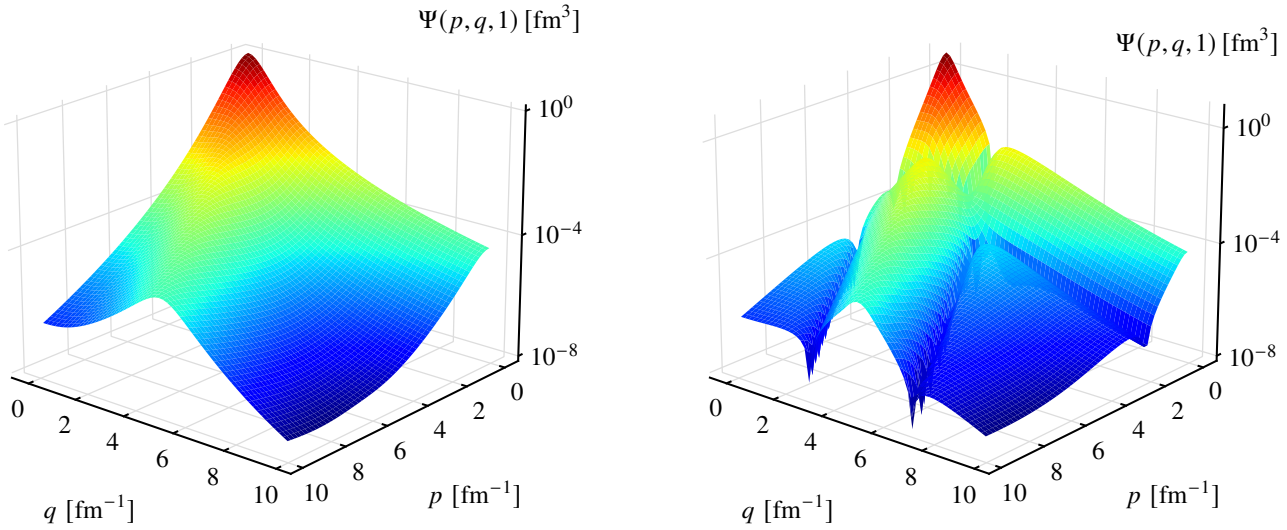


FIG. 10. Three-boson wave functions $\Psi(p,q,1)$ for the YAMA-23 (left) and the MT5 (right) potential in the 3D-approach.

[1] L. D. Faddeev, Zh. Eksp.. Teor. Fiz **39**, 1459 (1960).
[2] O. A. Yakubovsky, Sov. J. Nucl. Phys. **5**, 937 (1967).
[3] Ch. Elster, J. H. Thomas, and W. Glöckle, Few-Body Systems **24**, 55 (1998).
[4] Ch. Elster, W. Schadow, A. Nogga, and W. Glöckle, Few-Body Systems **27**, 83 (1999).
[5] W. Schadow, Ch. Elster, and W. Glöckle, Few-Body Systems **28**, 15 (2000).
[6] M. Polášek and M. Ingr and P. Čársky and J. Horáček, Phys. Rev. A **61**, 032701 (2000).
[7] J. Shertzer and A. Temkin, Phys. Rev. A **63**, 062714 (2001).
[8] G. L. Caia and V. Pascalutsa and L. E. Wright, Phys. Rev. C **69**, 034003 (2004).
[9] B. Kessler and G. L. Payne and W. N. Polyzou, Phys. Rev. C **70**, 034003 (2004).
[10] A. S. Kadyrov and I. Bray and A. T. Stelbovics and B. Saha, J. Phys. B: At. Mol. Opt. Phys. **38**, 509 (2005).
[11] H. Liu, Ch. Elster, and W. Glöckle, Phys. Rev. C **72**, 054003 (2005).
[12] G. Ramalho and A. Arriaga and M. T. Peña, Few-Body Systems **39**, 123 (2006).
[13] H. Liu, Ch. Elster, and W. Glöckle, Nucl. Phys. **A790**, 262c (2007).
[14] M. R. Hadizadeh and S. Bayegan, Few-Body Systems **40**, 171 (2007).
[15] M. Rodriguez-Gallardo and A. Deltuva and E. Cravo and R. Crespo and A. C. Fonseca, Phys. Rev. C **78**, 034602 (2008).
[16] M. R. Hadizadeh and S. Bayegan, Eur. Phys. J. A **36**, 201 (2008).
[17] S. Bayegan, M. R. Hadizadeh, and M. Harzchi, Phys. Rev. C **77**, 064005 (2008).
[18] M. Harzchi and S. Bayegan, Eur. Phys. J. **A46**, 271 (2010).
[19] W. Glöckle, Ch. Elster, J. Golak, R. Skibiński, H. Witała, and H. Kamada, Few-Body Systems **47**, 25 (2010).
[20] J. Golak, W. Glöckle, R. Skibiński, H. Witała, D. Rozpedzik, K. Topolnicki, I. Fachruddin, Ch. Elster, and A. Nogga, Phys. Rev. C **81**, 034006 (2010).
[21] J. Golak, K. Topolnicki, R. Skibiński, W. Glöckle, H. Kamada, and A. Nogga, Few-Body Systems **54**, 2427 (2013).
[22] M. A. Shalchi and S. Bayegan, Eur. Phys. J. **A48**, 6 (2012).
[23] S. Veerasamy and Ch. Elster and W. N. Polyzou, Few-Body Systems **54**, 2207 (2013).
[24] M. Harzchi and S. Bayegan, J. Theor. Appl. Phys. **8**, 112 (2014).
[25] Z. C. Kuruoğlu, Phys. Rev. E **94**, 053308 (2016).
[26] Y. Yamaguchi, Phys. Rev. **95**, 1628 (1954).
[27] R. A. Malfliet and J. A. Tjon, Nucl. Phys. **A127**, 161 (1969).
[28] L. N. G. Filon, Proc. Roy. Soc. Edinburgh **49**, 38 (1930).
[29] W. H. Press, S. A. Teukolsky, W. T. Vetterling, and B. P. Flannery, *Numerical Recipes: The Art of Scientific Computing*, 3rd ed. (Cambridge University Press, New York, NY, USA, 2007).
[30] E. O. Alt, P. Grassberger, and W. Sandhas, Nucl. Phys. **B2**, 167 (1967).
[31] W. Glöckle, *The Quantum Mechanical Few-Body Problem* (Springer-Verlag, Berlin-Heidelberg, 1983).
[32] D. Hüber, H. Witała, and W. Glöckle, Few-Body Systems **14**, 171 (1993).
[33] M. Mohammadzadeh, M. Radin, and M. R. Hadizadeh, Prog. Theor. Exp. Phys. **2024**, 013D03 (2024).
[34] H. Liu, Ch. Elster, and W. Glöckle, Few-Body Systems **33**, 241 (2003).
[35] W. Schadow, Few-Body Systems **67**, 31 (2026).
[36] H. Yukawa, Proc. Phys.-Math. Soc. (Japan) **17**, 48 (1935).
[37] W. E. Arnoldi, Q. Appl. Math. **9**, 17 (1951).
[38] A. Stadler, W. Glöckle, and P. U. Sauer, Phys. Rev. C **44**, 2319 (1991).
[39] W. Glöckle, *Computational Nuclear Physics I. Nuclear Structure, Edited by K. Langanke, J. A. Maruhn, and S. E. Koonin, pp 152* (Springer-Verlag, Berlin-Heidelberg, 1991).